

## Softness Ratio of SWIFT Gamma-ray Bursts and Relevant Correlations

FAN XU<sup>\*</sup>,<sup>1,2</sup> YONG-FENG HUANG<sup>\*</sup>,<sup>2,3</sup> LIANG LI,<sup>4,5,6</sup> JIN-JUN GENG,<sup>7</sup> XUE-FENG WU,<sup>7</sup> SONG-BO ZHANG,<sup>7</sup> CHEN DENG,<sup>2</sup>  
CHEN-RAN HU,<sup>2</sup> XIAO-FEI DONG,<sup>2</sup> AND HAO-XUAN GAO<sup>7</sup>

<sup>1</sup>Department of Physics, Anhui Normal University, Wuhu, Anhui 241002, People's Republic of China

<sup>2</sup>School of Astronomy and Space Science, Nanjing University, Nanjing 210023, People's Republic of China

<sup>3</sup>Key Laboratory of Modern Astronomy and Astrophysics (Nanjing University), Ministry of Education, People's Republic of China

<sup>4</sup>Institute of Fundamental Physics and Quantum Technology, Ningbo University, Ningbo, Zhejiang 315211, People's Republic of China

<sup>5</sup>School of Physical Science and Technology, Ningbo University, Ningbo, Zhejiang 315211, People's Republic of China

<sup>6</sup>INAF-Osservatorio Astronomico d'Abruzzo, Via M. Maggini snc, I-64100, Teramo, Italy

<sup>7</sup>Purple Mountain Observatory, Chinese Academy of Sciences, Nanjing 210023, People's Republic of China

(Received May 13, 2025; Revised May 13, 2025; Accepted XXX)

### ABSTRACT

The properties of X-ray flashes (XRFs) and X-ray rich gamma-ray bursts (XRRs) as compared with classical gamma-ray bursts (C-GRBs) have been widely discussed during the *Swift* era. It has been proposed that XRFs and XRRs are low-energy extensions of the GRB population so that they should follow similar correlations. To further examine this idea, we collect a sample of 303 GRBs detected by *Swift* over the past two decades, all of which have reliable redshifts and spectral parameters. The bursts are classified into XRFs, XRRs, and C-GRBs based on their softness ratio (SR), which is calculated by dividing the 25 – 50 keV fluence with the 50 – 100 keV fluence. A strong correlation is found among the isotropic energy  $E_{\text{iso}}$ , peak luminosity  $L_{\text{p}}$ , and rest frame burst duration  $T_{90,\text{rest}}$ , i.e.,  $E_{\text{iso}} \propto L_{\text{p}}^{0.88 \pm 0.02} T_{90,\text{rest}}^{0.58 \pm 0.02}$ . Additionally, two tight three-parameter correlations involving SR and the rest-frame peak energy  $E_{\text{p}}$  are also derived, i.e.  $E_{\text{p}} \propto E_{\text{iso}}^{0.20 \pm 0.02} \text{SR}^{-2.27 \pm 0.15}$  and  $E_{\text{p}} \propto L_{\text{p}}^{0.17 \pm 0.02} \text{SR}^{-2.33 \pm 0.14}$ . It is interesting to note that XRFs, XRRs, and C-GRBs all follow the above correlations. The implications of these correlations and their potential application in cosmology are discussed.

**Keywords:** Gamma-ray bursts(629); High energy astrophysics(739); Astronomy data analysis(1858); Non-thermal radiation sources(1119); Markov chain Monte Carlo(1889)

### 1. INTRODUCTION

The prompt emission of gamma-ray bursts (GRBs) spans a broad energy range from keV to GeV (Abdo et al. 2009; Zhang et al. 2011). It is found that the softness ratios (SRs), defined as the fluence ratio between the X-ray and gamma-ray bands, vary significantly among bursts (Barraud et al. 2003; Sakamoto et al. 2005). Bursts with softer spectra are classified as X-ray flashes (XRFs; Heise et al. (2001); Kippen et al. (2001)), while those with harder spectra are referred to as classical GRBs (C-GRBs; Sakamoto et al. 2008). Between these two categories lies the intermediate class of X-ray-rich GRBs (XRRs; Heise et al. (2001)). Generally speaking, XRFs and XRRs are regarded as low-energy extensions of the GRB population (Barraud et al. 2005).

The origin of XRFs and XRRs remains a topic of debate (Zhang & Mészáros 2002; Sakamoto et al. 2008). One possible explanation is that intrinsic factors cause the differences between XRFs, XRRs, and C-GRBs. It has been argued that XRFs may originate from GRB jets with lower Lorentz factors, namely dirty fireballs (Dermer et al. 1999; Huang et al. 2002; Sun et al. 2024; Geng et al. 2025). Alternatively, they might from jets with low radiation efficiency (Mochkovitch et al. 2004; Barraud et al. 2005). Additionally, it is proposed that non-thermal emission from the dissipative process of the photosphere could account for the strong X-ray emission in XRFs and XRRs (Ramirez-Ruiz 2005; Pe'er et al. 2006). On the other hand, extrinsic factors have also been considered. Several groups have investigated the effects of viewing angle or structured jets on the observed softness of GRBs (Yamazaki et al. 2002, 2004; Zhang et al. 2004; Lamb et al. 2004a; Granot et al. 2005; Xu et al. 2023b; O'Connor

\*Corresponding author: Fan Xu (fanxu@ahnu.edu.cn), Yong-Feng Huang (hyf@nju.edu.cn)

et al. 2024; Gao et al. 2024). Interestingly, these models are also commonly invoked to explain orphan afterglows (Rhoads 1997; Huang et al. 2002; Urata et al. 2015; Xu et al. 2023a; Ye et al. 2024; Li et al. 2024b).

The parameter distributions and correlations of XRFs, XRRs, and C-GRBs have also been investigated in depth by various researchers. No systematic differences are found for these three subgroups in their low-energy photon indices, high-energy photon indices, or durations (Kippen et al. 2003; Sakamoto et al. 2005, 2008). Additionally, all the three categories appear to follow similar empirical correlations. For example, an anti-correlation has been found between SR and the peak energy of the  $\nu F_\nu$  spectra,  $E_{p,obs}$  (Sakamoto et al. 2005, 2008; Katsukura et al. 2020). It indicates that XRFs tend to have lower  $E_{p,obs}$ . Furthermore, the rest-frame peak energy  $E_p$  and the isotropic energy  $E_{iso}$  exhibit a robust relationship, known as the  $E_p - E_{iso}$  (Amati) correlation (Amati et al. 2002). This correlation has been shown to hold consistently across XRFs, XRRs, and C-GRBs (Lamb et al. 2004b; Sakamoto et al. 2006; Amati 2006; Bi et al. 2018; Katsukura et al. 2020). Several other correlations have also been explored, though their robustness is often limited by the sample size and the uncertainty of the data.

In this study, we conduct a detailed analysis of GRB prompt emission correlations, paying special attention to GRBs that have well-constrained spectra and redshift measurements. The GRB data in our sample are taken from the third *Swift* Burst Alert Telescope (BAT; Barthelmy et al. (2005a)) GRB catalog<sup>1</sup> (hereafter the BAT3 catalog; Lien et al. (2016)), including 303 GRBs observed between 2005 January and 2024 September. The *Swift* mission (Gehrels et al. 2004), launched in 2004 with an initial two-year operational plan, has far exceeded expectations. Over the past two decades, it has provided groundbreaking GRB observations and revolutionized our understanding of GRBs (e.g., Barthelmy et al. (2005b); Gehrels et al. (2005); Villasenor et al. (2005); Zhang et al. (2006); Gehrels et al. (2006); Greiner et al. (2009); Cucchiara et al. (2011); Jin et al. (2016)). Using this rich data set, we will explore potential correlations among various parameter pairs or combinations, which may offer new insights into GRB physics and could be applied in various fields such as cosmology.

The structure of this paper is as follows. In Section 2, we describe our sample selection criteria and data reduction procedures. Section 3 presents the statistical analysis and results. In Section 4, we summarize our conclusions and discuss their implications. Throughout this study, a flat  $\Lambda$ CDM model with  $H_0 = 67.8 \text{ km s}^{-1} \text{ Mpc}^{-1}$  and  $\Omega_m = 0.308$  is assumed (Planck Collaboration et al. 2016).

## 2. SAMPLE SELECTION AND DATA ANALYZE

The BAT3 catalog contains a total of 1585 GRBs detected by *Swift* over the past two decades (Lien et al. 2016). From this catalog, we built our sample based on three main criteria. (1) Some key observational parameters, including the GRB duration  $T_{90}$ , fluence, and peak flux, should be available. This ensures that we can perform reliable correlation analyses. (2) The redshift should have been measured for each burst. (3) The photon index and peak energy ( $E_{p,obs}$ ) should be well-constrained for the event, as  $E_{p,obs}$  is a key parameter in GRB correlation studies. Additionally, accurate spectral information is necessary for performing k-corrections. While the relatively narrow energy range of *Swift* leads to difficulty in measuring  $E_{p,obs}$  accurately, we referred to the spectral parameters available from several other sources, which include the *Fermi* online catalog<sup>2</sup> (Gruber et al. 2014; von Kienlin et al. 2014; Narayana Bhat et al. 2016; von Kienlin et al. 2020), the Konus-Wind online catalog<sup>3</sup> (Tsvetkova et al. 2017, 2021), and the General Coordinate Network (GCN) Circulars<sup>4</sup>. 15 GRBs with well-constrained cut-off power-law spectra from the BAT3 catalog are also included in our sample. After applying these criteria, we finally built our sample that includes 303 GRBs. The observational parameters of these bursts taken from the *Swift* database are presented in Table 1, while the spectral parameters of each burst are listed in Table 2.

In Table 1, we categorize our sample into long GRBs (LGRBs) with  $T_{90} > 2 \text{ s}$  and short GRBs (SGRBs) with  $T_{90} < 2 \text{ s}$ . Note that six well-known GRBs with extended emission (i.e. GRBs 061006, 071227, 070714B, 090510, 100816A, and 160410A), which have  $T_{90} > 2 \text{ s}$ , are classified as SGRBs instead of LGRBs (van Putten et al. 2014; Lien et al. 2016; Minaev & Pozanenko 2020; Li et al. 2021). This results in 21 SGRBs and 282 LGRBs included in our sample. This classification of long and short events proves important in subsequent correlation analysis, as SGRBs exhibit distinct behaviors compared to LGRBs in some correlations.

We classify XRFs, XRRs, and C-GRBs based on the following criteria proposed by Sakamoto et al. (2008)

$$\begin{aligned} S(25 - 50 \text{ keV})/S(50 - 100 \text{ keV}) &\leq 0.72 && \text{(C - GRB)}, \\ 0.72 < S(25 - 50 \text{ keV})/S(50 - 100 \text{ keV}) &\leq 1.32 && \text{(XRR)}, \\ 1.32 < S(25 - 50 \text{ keV})/S(50 - 100 \text{ keV}) &&& \text{(XRF)}. \end{aligned} \tag{1}$$

<sup>1</sup> [https://swift.gsfc.nasa.gov/results/batgrbeat/index\\_tables.html](https://swift.gsfc.nasa.gov/results/batgrbeat/index_tables.html)

<sup>2</sup> <https://heasarc.gsfc.nasa.gov/W3Browse/fermi/fermigbrst.html>

<sup>3</sup> <https://www.ioffe.ru/LEA/catalogs.html>

<sup>4</sup> <https://gcn.gsfc.nasa.gov/circulars>

We define the softness ratio as  $SR = S(25 - 50 \text{ keV})/S(50 - 100 \text{ keV})$ , which is the ratio of fluence in the 25 – 50 keV band ( $S(25 - 50 \text{ keV})$ ) with respect to that in 50 – 100 keV ( $S(50 - 100 \text{ keV})$ ). The values of  $S(25 - 50 \text{ keV})$  and  $S(50 - 100 \text{ keV})$  are taken from the BAT3 catalog (Lien et al. 2016). Among the 303 GRBs in our sample, we have 5 XRFs, 167 XRRs, and 131 C-GRBs according to the above definition. The distribution of SR for the entire sample is shown in Figure 2. The number of XRFs in our sample is quite limited due to our requirement for a well-constrained spectrum. XRFs generally have  $E_{p,\text{obs}} < 30 \text{ keV}$ , which is very close to the low-energy threshold of most GRB detectors (e.g., *Fermi*/GBM, *Konus-Wind*, and *Swift*/BAT). Therefore the spectral parameters of XRFs are often poorly constrained. In contrast, the proportion of XRRs (55%) and C-GRBs (43%) in our sample are comparable, which is consistent with previous studies (Sakamoto et al. 2008; Bi et al. 2018; Katsukura et al. 2020).

With the energy fluence listed in Table 1, we derive the isotropic energy of the prompt emission as

$$E_{\text{iso}} = \frac{4\pi D_L^2(z)S(15 - 150 \text{ keV})k}{1+z}, \quad (2)$$

where  $S(15 - 150 \text{ keV})$  is the energy fluence in 15 – 150 keV band,  $z$  is the redshift and  $D_L$  is the luminosity distance.  $k$  represents the k-correction factor, which adjusts the energy to a common cosmological rest-frame band of 1 – 10<sup>4</sup> keV. To calculate the k-correction factor, we use the spectra information listed in Table 2. For each burst in our sample with a photon spectrum of  $N(E)$ , the k-correction factor  $k$  is given by

$$k = \frac{\int_{1/(1+z)}^{10^4/(1+z)} EN(E)dE}{\int_{15}^{150} EN(E)dE}. \quad (3)$$

We can also calculate the isotropic peak luminosity with  $k$ , i.e.,

$$L_p = 4\pi D_L^2 F(15 - 150 \text{ keV})k, \quad (4)$$

where  $F(15 - 150 \text{ keV})$  is the peak energy flux in 15 – 150 keV band.

The parameters relevant to our correlation study are summarized in Table 3. These include the softness ratio SR, the rest frame burst duration  $T_{90,\text{rest}} = T_{90}/(1+z)$ , the isotropic energy  $E_{\text{iso}}$ , the isotropic peak luminosity  $L_p$ , and the rest frame peak energy  $E_p = E_{p,\text{obs}} \times (1+z)$ . With these data, we explore the parameter distributions and correlations for XRFs, XRRs, and C-GRBs. The results of these analyses are presented in the following section.

### 3. RESULTS

#### 3.1. Distributions of Parameters

In Figure 2, we present the distributions of spectral parameters for XRFs, XRRs, and C-GRBs. As shown in Figure 2(c), the observed peak energy varies significantly among XRFs, XRRs, and C-GRBs. This is consistent with previous studies (Sakamoto et al. 2005, 2008; Bi et al. 2018; Katsukura et al. 2020). The low-energy index  $\alpha$  in our sample ranges from  $-1.84$  to  $0.5$  and peaks around  $-1$ . The distribution of the high energy index  $\beta$  in our sample clusters around  $-2.5$  and ranges in  $(-3.52, -1.58)$ . Notably, as shown in Figure 2(a), the  $\alpha$  values of XRRs are systematically lower than those of C-GRBs. However, no significant difference is observed in the high-energy index. This contrasts with earlier studies (Kippen et al. 2003; Sakamoto et al. 2005), where no systematic differences were found for both  $\alpha$  and  $\beta$ . The lower values of  $\alpha$  for XRRs are consistent with their classification as being softer than C-GRBs in the low-energy band.

To further investigate the difference of  $\alpha$  among XRFs, XRRs, and C-GRBs, we have performed pairwise Kolmogorov-Smirnov (K-S) tests. The results are presented in Table 4. For XRRs and C-GRBs, we find the K-S test probability ( $P$ ) of  $\alpha$  is  $3.70 \times 10^{-13}$ , indicating a significant difference in the low-energy indices between the two categories. In contrast, the K-S test probability of  $\beta$  is 0.8, suggesting that the high-energy indices of XRRs and C-GRBs are statistically indistinguishable. Since the sample size of XRFs is too small, K-S tests involving XRFs fail to generate any statistically reliable conclusions.

K-S tests are also performed to examine the statistical difference between LGRBs and SGRBs. It is found that both the observed peak energy ( $E_{p,\text{obs}}$ ) and the low-energy index ( $\alpha$ ) differ significantly between LGRBs and SGRBs, with  $P \sim 0.00032$  and  $P \sim 3.10 \times 10^{-05}$ , respectively. Specifically, SGRBs tend to exhibit higher  $E_{p,\text{obs}}$  and  $\alpha$ , suggesting that they are harder than LGRBs. However, since none of the SGRBs in our sample have well-constrained  $\beta$  values, we cannot assess whether the high-energy index differs between LGRBs and SGRBs.

In Table 4, we also present the  $P$ -values for key parameters relevant to our correlation study. For instance, the rest-frame peak energy  $E_p$  is similar for LGRBs and SGRBs ( $P = 0.26$ ). This could result from a selection effect, as SGRBs usually have

lower redshifts and higher observed peak energies compared to LGRBs. In contrast, both the isotropic energy ( $E_{\text{iso}}$ ) and the peak luminosity ( $L_p$ ) of LGRBs are systematically higher than that of SGRBs. Furthermore, C-GRBs exhibit larger  $E_{\text{iso}}$  and  $L_p$  than XRRs. However, the rest frame durations of XRRs and C-GRBs are very similar and indistinguishable.

### 3.2. Correlations among parameters

We have explored potential correlations between various parameter combinations. To get the best-fit expressions for the correlations, the Markov chain Monte Carlo (MCMC) algorithm is used. The Spearman correlation coefficient  $\rho$  and the corresponding chance probability  $p$  are calculated for the best-fit curve. The results are summarized in Table 5.

#### 3.2.1. The Correlations between $E_{\text{iso}}$ , $L_p$ , and $T_{90,\text{rest}}$

Previous studies have revealed a potential correlation between  $E_{\text{iso}}$  and  $L_p$  (Lamb et al. 2005; Ghirlanda et al. 2005). In Figure 3, we plot  $E_{\text{iso}}$  versus  $L_p$  for all GRBs in our samples. A clear positive correlation is observed, indicating that more energetic bursts tend to have a higher peak luminosity, which aligns with expectations. The best-fit correlation is  $L_p \propto E_{\text{iso}}^{0.85 \pm 0.03}$ , with  $\rho = 0.85$  and  $p = 7.60 \times 10^{-84}$ .

However, the intrinsic scatter of this correlation is relatively large ( $\sigma_{\text{in}} = 0.46 \pm 0.02$ ). This may be due to the fact that the total energy released in a burst is not solely determined by the peak luminosity but also influenced by the burst duration, i.e.,  $E_{\text{iso}} \sim L_p \times T_{90,\text{rest}}$ . Inspired by this equation, we have explored the three-parameter correlation involving  $E_{\text{iso}}$ ,  $L_p$ , and  $T_{90,\text{rest}}$ . The best-fit result is  $E_{\text{iso}} \propto L_p^{0.88 \pm 0.02} T_{90,\text{rest}}^{0.58 \pm 0.02}$  with a much smaller intrinsic scatter of  $\sigma_{\text{in}} = 0.24 \pm 0.01$  as compared with the two-parameter  $E_{\text{iso}} - L_p$  correlation. The Spearman correlation coefficient for this three-parameter relation is  $\rho = 0.95$ , with a probability of  $p = 6.20 \times 10^{-153}$ , suggesting a strong correlation among  $E_{\text{iso}}$ ,  $L_p$ , and  $T_{90,\text{rest}}$ . Our fitting result is illustrated in Figure 4.

From Figure 4, we see that both LGRBs and SGRBs, as well as XRFs, XRRs, and C-GRBs, are tightly distributed along the best-fit line. It is striking to see that this correlation holds even with a large sample size of 303 GRBs, and it applies for all these different subclasses of events. The power-law index of  $L_p$  in the correlation is close to 1, which is consistent with the expectation from  $E_{\text{iso}} \sim L_p \times T_{90,\text{rest}}$ . However, the index of  $T_{90,\text{rest}}$  is around 0.6, which is much less than 1. This deviation can be attributed to the multiple spike structure often observed in the GRB light curves of prompt emission. Consequently, the isotropic energy integrated over the burst duration ( $E_{\text{iso}}$ ) is typically smaller than  $L_p \times T_{90,\text{rest}}$ .

Interestingly, Xu & Huang (2012) found a tight  $L$ - $T$ - $E$  correlation for GRBs with a plateau in the X-ray afterglow light curve. It is expressed as  $L_X \propto T_a^{-0.99} E_{\text{iso}}^{0.86}$  (Tang et al. 2019; Zhao et al. 2019; Deng et al. 2023), where  $T_a$  is the plateau duration and  $L_X$  is the X-ray luminosity of the plateau. Such an  $L$ - $T$ - $E$  correlation involving  $L_p$ ,  $T_{90,\text{rest}}$  and  $E_{\text{iso}}$  is further confirmed in our current study.

Additionally, we have also explored other three parameter correlations such as  $E_{\text{iso}} - T_{90,\text{rest}} - E_p$ ,  $L_p - T_{90,\text{rest}} - E_p$ , and  $E_{\text{iso}} - L_p - E_p$ . The best-fit results are shown in Figure 5. The intrinsic scatters of these correlations are around 0.3, with the Spearman correlation coefficients of approximately 0.6. It indicates that while these parameters are truly correlated, the significance of these correlations is generally not high. These correlations are likely connected with the well-known Amati correlation ( $E_{\text{iso}} - E_p$ ) (Amati et al. 2002) and the Yonetoku correlation ( $L_p - E_p$ ) (Yonetoku et al. 2004).

#### 3.2.2. The $E_{\text{iso}}$ -SR- $E_p$ and $L_p$ -SR- $E_p$ Correlations

It has been proposed that a strong correlation should exist between the softness ratio and the peak energy (Sakamoto et al. 2005, 2008; Katsukura et al. 2020). Sakamoto et al. (2008) calculated the theoretical SR curve as a function of  $E_{p,\text{obs}}$ . They used the Band function to describe the  $\gamma$ -ray spectrum, taking the power-law indices as  $\alpha = -1$  and  $\beta = -2.5$ . It was found that the observational data points distributed tightly around this curve. The scatter of this correlation is primarily attributed to variations of  $\alpha$  and  $\beta$  for individual bursts. In Figure 6(a), we plot  $E_p$  versus SR for the GRBs in our sample. We can also see a strong inverse relationship between the two parameters. The best-fit result is  $E_p \propto \text{SR}^{-2.91 \pm 0.16}$ , with an intrinsic scatter of  $\sigma_{\text{in}} = 0.21 \pm 0.01$ . The Spearman correlation coefficient is  $\rho = -0.74$ , with a probability of  $p = 1.30 \times 10^{-53}$ . Such an anti-correlation is easy to understand since a higher SR value corresponds to a softer spectrum and a lower peak energy. In Figure 6, we also show the  $\text{SR} - E_{\text{iso}}$  and  $\text{SR} - L_p$  correlations, both of which are relatively diffuse.

On the other hand, the three-parameter correlations of  $E_{\text{iso}} - \text{SR} - E_p$  and  $L_p - \text{SR} - E_p$  are found to be very tight. The best-fit results for these two three-parameter correlations are shown in Figure 7. Our best-fit expressions are  $E_p \propto E_{\text{iso}}^{0.18 \pm 0.02} \text{SR}^{-2.40 \pm 0.13}$ , with  $\rho = 0.84$  and  $p = 2.70 \times 10^{-80}$ , and  $E_p \propto L_p^{0.17 \pm 0.02} \text{SR}^{-2.33 \pm 0.14}$ , with  $\rho = 0.84$  and  $p = 1.50 \times 10^{-80}$ .

Notably, SGRBs 090510 and 071227 appear as outliers in both correlations. It indicates that LGRBs and SGRBs may follow different  $E_{\text{iso}} - \text{SR} - E_p$  and  $L_p - \text{SR} - E_p$  correlations. To be more specific, we examine these two correlations for LGRBs in

our sample. For the  $E_{\text{iso}} - \text{SR} - E_{\text{p}}$  correlation, we get  $E_{\text{p}} \propto E_{\text{iso}}^{0.20 \pm 0.02} \text{SR}^{-2.27 \pm 0.15}$ , with  $\sigma_{\text{in}} = 0.16 \pm 0.01$ . For the  $L_{\text{p}} - \text{SR} - E_{\text{p}}$  correlation, we obtain  $E_{\text{p}} \propto L_{\text{p}}^{0.17 \pm 0.02} \text{SR}^{-2.33 \pm 0.14}$ , with  $\sigma_{\text{in}} = 0.17 \pm 0.01$ . The best-fit results are shown in Figure 8. Again, we see that XRFs, XRRs, and C-GRBs follow the same tight correlation.

We have also examined the Amati correlation and the Yonetoku correlation for LGRBs. The best-fit results are illustrated in Figure 9. We see that most GRBs follow the best-fit lines represented by  $E_{\text{p}} \propto E_{\text{iso}}^{0.49 \pm 0.02}$  and  $E_{\text{p}} \propto L_{\text{p}}^{0.50 \pm 0.02}$ . However, a few low-luminosity XRRs and C-GRBs seem to follow a shallower track with significantly smaller power-law indices. Currently, the origin of low-luminosity GRBs is still under debate (Dong et al. 2023). One possibility is that they form a distinct GRB population (Liang et al. 2007). Another possibility is that they may be normal GRB outflows observed off-axis (Granot et al. 2002; Huang et al. 2002; Yamazaki et al. 2003; Xu et al. 2023b; Li et al. 2024c). Anyway, they exhibit some different properties compared to high-luminosity GRBs, as shown in Figure 9.

Comparing Figure 8 with Figure 9, we find that our three-parameter correlations are much tighter. These strong three-parameter correlations highlight the importance of SR in linking  $E_{\text{p}}$  with both  $E_{\text{iso}}$  and  $L_{\text{p}}$ . Moreover, we have also explored whether additional parameters could further tighten our correlations. For example, we examined possible connection in the four parameters of  $E_{\text{iso}} - T_{90,\text{rest}} - \text{SR} - E_{\text{p}}$ , and in  $L_{\text{p}} - T_{90,\text{rest}} - \text{SR} - E_{\text{p}}$ . The best-fit results correspond to an intrinsic scatter of  $\sigma_{\text{in}} \sim 0.16$  and  $\rho = 0.86$  for both correlations and the power-law index of  $T_{90,\text{rest}}$  is very close to 0. It means that the burst duration plays a minor role in these correlations so that these four-parameter correlations are not preferred.

### 3.2.3. Redshift evolution

The parameters discussed above may be affected by selection biases due to instrumental thresholds and redshift evolution (Dainotti et al. 2013, 2015). The redshift evolution may distort the statistical correlations (Dainotti et al. 2022a). To mitigate these biases in truncated datasets, the method proposed by Efron & Petrosian (1992) is commonly used (see also Dainotti et al. (2017b, 2020a); Xu et al. (2021)). It applies a modified version of Kendall's  $\tau$  statistics and can effectively remove the redshift evolution from the parameters (Dainotti et al. 2021).

For a selected parameter  $x$ , we take the redshift evolution form as  $g(z) = (1+z)^{k_x}$ , where  $k_x$  is the evolutionary coefficient. The de-evolved parameter is then given by  $x' = x/g(z)$  (Dainotti et al. 2023; Lenart et al. 2025). For the SR parameter, we expect no redshift evolution, as there is no redshift-related term in its equation. For other parameters, we use the results summarized in Table 2 by Dainotti et al. (2022b) as proxies. After de-evolving the parameters, we re-fit the correlations and summarize the results in Table 6.

Our analysis shows that most correlations exhibit a smaller intrinsic scatter after accounting for redshift effects. It indicates that these correlations become tighter when the redshift evolution is corrected. In contrast, a few correlations exhibit a slight increase in scatter following the correction. In particular, the  $E_{\text{iso}} - L_{\text{p}} - T_{90,\text{rest}}$  correlation shows a larger intrinsic scatter for both the entire sample and the LGRB sample. Overall, we note that for correlations with a relatively small intrinsic scatter ( $\sigma_{\text{in}} \lesssim 0.3$ ), the redshift correction appears to have only a modest effect on their tightness.

## 4. CONCLUSIONS AND DISCUSSION

In this study, we collect 303 GRBs detected by *Swift* with known redshift and well-constrained spectra parameters. A systematical statistical analysis is carried out based on the sample. The GRBs are categorized into subgroups of XRFs, XRRs, and C-GRBs, as well as LGRBs and SGRBs, to investigate and compare their difference in parameter distributions and correlations. Based on the K-S tests, it is found that XRRs and C-GRBs exhibit obviously different low-energy indices and peak energies. While SGRBs typically have lower redshifts and higher observed peak energies, their rest-frame peak energies are similar to that of LGRBs. A strong correlation is found among the three parameters of  $L_{\text{p}}$ ,  $T_{90,\text{rest}}$ , and  $E_{\text{iso}}$ . The best-fit expression is  $E_{\text{iso}} \propto L_{\text{p}}^{0.88 \pm 0.02} T_{90,\text{rest}}^{0.58 \pm 0.02}$ , with an intrinsic scatter of  $\sigma_{\text{in}} = 0.24 \pm 0.01$ . This correlation holds for various subgroups, including LGRBs and SGRBs, as well as XRFs, XRRs, and C-GRBs. Additionally, two very tight correlations involving the softness ratio (SR) are identified. For LGRBs, we obtain  $E_{\text{p}} \propto E_{\text{iso}}^{0.20 \pm 0.02} \text{SR}^{-2.27 \pm 0.15}$  and  $E_{\text{p}} \propto L_{\text{p}}^{0.17 \pm 0.02} \text{SR}^{-2.33 \pm 0.14}$ . These three-parameter correlations could be regarded as an extension of the well-known Amati and Yonetoku correlations, but are interestingly much tighter, with an intrinsic scatter of  $\sigma_{\text{in}} \sim 0.16$ .

It is found that XRFs, XRRs, and C-GRBs follow similar correlations involving prompt emission parameters. It supports the idea that XRFs and XRRs are low-energy extensions of the GRB population. The  $L_{\text{p}} - T_{90,\text{rest}} - E_{\text{iso}}$  correlation involves parameters that are closely related to the temporal property of GRB prompt emission. The existence of this correlation indicates that GRB prompt emission light curves may share similar pulse profiles despite their apparent complexity. For instance, a fast-rising exponential-decay profile may dominate the light curves of most GRBs (Norris et al. 1996). Furthermore, since both SGRBs and LGRBs adhere to this correlation, these similar structures may exist in both SGRBs and LGRBs.

In our study, the softness ratio (SR) is defined as the ratio of fluence in the 25 – 50 keV band with respect to that in the 50 – 100 keV band. The logarithm value of SR employed in our correlation analysis is somewhat similar to the color parameter used in the standard candle correlation of Type Ia supernovae (SNe Ia). In the Tripp formula for SNe Ia, a color term of  $b(B-V)$  is included, where  $b$  is the correlation coefficient and  $(B-V)$  represents the color index (Tripp 1998). The inclusion of this term significantly tightens the SNe Ia correlation. Similarly, we find that both the Amati and Yonetoku correlations become much tighter when the SR parameter is included.

While we discuss the correlation concerning the prompt emission phase of GRBs, several tight correlations have also been revealed in their afterglow phase, particularly those associated with plateau features. Dainotti et al. (2008) first discovered a correlation between the X-ray plateau luminosity ( $L_X$ ) and its duration ( $T_a$ ), which is also known as the Dainotti relation (see also (Dainotti et al. 2013)). Building on this, Dainotti et al. (2016) introduced a three-parameter correlation that includes the prompt peak luminosity ( $L_p$ ) in addition to  $L_X$  and  $T_a$ . They demonstrated that this extended correlation (the Dainotti fundamental plane correlation) becomes even tighter when applied to class-specific GRB samples (Dainotti et al. 2016, 2017a). To further reduce observational biases, Dainotti et al. (2020a) applied the Efron & Petrosian (1992) method to remove redshift evolution effects from each parameter. This analysis yielded a refined relation:  $L_X \propto T_a^{-0.86 \pm 0.13} L_p^{0.56 \pm 0.12}$ , with an intrinsic scatter of about 0.22. Notably, this correlation has also proven useful for distinguishing between different GRB subclasses (Lenart et al. 2025). Similar correlations have been noticed in GRBs exhibiting optical plateaus, in both two-parameter and three-parameter forms (Dainotti et al. 2020b, 2022d,c) as well as in those exhibiting radio plateaus (Levine et al. 2022).

These tight correlations offer valuable opportunities for cosmological applications, further strengthen GRBs as cosmological probes (Dai et al. 2004; Wang et al. 2016; Dainotti et al. 2022b; Liang et al. 2022; Wang et al. 2022; Jia et al. 2022; Dainotti et al. 2023; Tian et al. 2023; Hu & Wang 2023; Li et al. 2024a). In particular, these GRB correlations could provide an independent measurement of the Hubble constant. Furthermore, GRBs at high redshifts could potentially fill the redshift gap between SNe Ia and the cosmic microwave background (Xu et al. 2021).

However, a significant limitation is that the redshift of many GRBs, especially those at high redshift, is still unknown due to the difficulty in observing their host galaxies. To compensate for this weakness, GRB correlations have been used to estimate pseudo-redshifts (Yonetoku et al. 2004; Dainotti et al. 2011; Deng et al. 2023), though the accuracy of this approach remains limited. An alternative solution is offered by machine learning (Morgan et al. 2012; Ukwatta et al. 2016). Recently, Dainotti et al. (2024a) employed a supervised statistical learning model that incorporates features from both the prompt and afterglow phases. Their predicted redshift shows strong correlation with the observed redshift, validating its reliability (see also Dainotti et al. (2024b, 2025)). Based on this framework, Narendra et al. (2024) released a publicly available Web-App for GRB redshift estimation, making the approach more convenient.

The number of XRFs in our sample is still very limited, primarily due to the lack of well-constrained spectral parameters of many GRBs. The peak energy of XRFs is typically very close to the low-energy threshold of most GRB detectors. Luckily, the *Einstein Probe* (*EP*; Yuan et al. (2022)) launched in 2024 operates in the soft X-ray band, offering new opportunities for the study of XRFs. The Wide-field X-ray Telescope (WXT, 0.5 – 4 keV) onboard *EP* has a sensitivity of  $(2 - 3) \times 10^{-11}$  erg cm<sup>-2</sup> s<sup>-1</sup> at 1 ks exposure, which is more than an order of magnitude better than that of current orbiting instruments (Gao et al. 2024; Zhang et al. 2025). A number of GRBs have already been recorded by *EP*/WXT (Yin et al. 2024; Zhou et al. 2024a,b; Zhang et al. 2025). Another prominent satellite is the *Space-based multi-band astronomical Variable Objects Monitor* (*SVOM*; Wei et al. (2016)) satellite which was launched in 2024. The ECLAIRS telescope and Gamma-Ray Monitor (GRM) onboard *SVOM* are designed to observe GRB prompt emission in the 4 – 150 keV and 15 – 5000 keV energy bands, respectively (Wang et al. 2024). With the help of *EP* and *SVOM*, we would expect more XRFs with well-constrained spectral parameters. The enlarged sample will allow for further testing of the robustness of the correlations revealed in this study.

#### ACKNOWLEDGMENTS

This study is supported by National Key R&D Program of China (2021YFA0718500), by National SKA Program of China No. 2020SKA0120300, and by the National Natural Science Foundation of China (Grant Nos. 12233002, 12273113). YFH also acknowledges the support from the Xinjiang Tianchi Program. JJG acknowledges support from the Youth Innovation Promotion Association (2023331). This work made use of data supplied by the UK *Swift* Science Data Centre at the University of Leicester and the *Swift* satellite.

#### REFERENCES

- Abdo, A. A., Ackermann, M., Arimoto, M., et al. 2009, *Science*, 323, 1688, doi: [10.1126/science.1169101](https://doi.org/10.1126/science.1169101)
- Amati, L. 2006, *MNRAS*, 372, 233, doi: [10.1111/j.1365-2966.2006.10840.x](https://doi.org/10.1111/j.1365-2966.2006.10840.x)

- Amati, L., Frontera, F., Tavani, M., et al. 2002, *A&A*, 390, 81, doi: [10.1051/0004-6361:20020722](https://doi.org/10.1051/0004-6361:20020722)
- Band, D., Matteson, J., Ford, L., et al. 1993, *ApJ*, 413, 281, doi: [10.1086/172995](https://doi.org/10.1086/172995)
- Barraud, C., Daigne, F., Mochkovitch, R., & Atteia, J. L. 2005, *A&A*, 440, 809, doi: [10.1051/0004-6361:20041572](https://doi.org/10.1051/0004-6361:20041572)
- Barraud, C., Olive, J. F., Lestrade, J. P., et al. 2003, *A&A*, 400, 1021, doi: [10.1051/0004-6361:20030074](https://doi.org/10.1051/0004-6361:20030074)
- Barthelmy, S. D., Barbier, L. M., Cummings, J. R., et al. 2005a, *SSRv*, 120, 143, doi: [10.1007/s11214-005-5096-3](https://doi.org/10.1007/s11214-005-5096-3)
- Barthelmy, S. D., Chincarini, G., Burrows, D. N., et al. 2005b, *Nature*, 438, 994, doi: [10.1038/nature04392](https://doi.org/10.1038/nature04392)
- Bi, X., Mao, J., Liu, C., & Bai, J.-M. 2018, *ApJ*, 866, 97, doi: [10.3847/1538-4357/aadcf8](https://doi.org/10.3847/1538-4357/aadcf8)
- Bissaldi, E., McBreen, S., & Connaughton, V. 2008a, *GRB Coordinates Network*, 8369, 1
- Bissaldi, E., McBreen, S., Wilson-Hodge, C. A., & von Kienlin, A. 2008b, *GRB Coordinates Network*, 8263, 1
- Bissaldi, E., Veres, P., & Fermi GBM Team. 2019, *GRB Coordinates Network*, 26000, 1
- Bissaldi, E., Veres, P., Meegan, C., & Fermi GBM Team. 2023, *GRB Coordinates Network*, 35369, 1
- Cucchiara, A., Levan, A. J., Fox, D. B., et al. 2011, *ApJ*, 736, 7, doi: [10.1088/0004-637X/736/1/7](https://doi.org/10.1088/0004-637X/736/1/7)
- Dai, Z. G., Liang, E. W., & Xu, D. 2004, *ApJL*, 612, L101, doi: [10.1086/424694](https://doi.org/10.1086/424694)
- Dainotti, M., Levine, D., Fraija, N., & Chandra, P. 2021, *Galaxies*, 9, 95, doi: [10.3390/galaxies9040095](https://doi.org/10.3390/galaxies9040095)
- Dainotti, M. G., Bargiacchi, G., Lenart, A. L., et al. 2022a, *ApJ*, 931, 106, doi: [10.3847/1538-4357/ac6593](https://doi.org/10.3847/1538-4357/ac6593)
- Dainotti, M. G., Cardone, V. F., & Capozziello, S. 2008, *MNRAS*, 391, L79, doi: [10.1111/j.1745-3933.2008.00560.x](https://doi.org/10.1111/j.1745-3933.2008.00560.x)
- Dainotti, M. G., De Simone, B., Islam, K. M., et al. 2022b, *ApJ*, 938, 41, doi: [10.3847/1538-4357/ac8b77](https://doi.org/10.3847/1538-4357/ac8b77)
- Dainotti, M. G., Del Vecchio, R., Shigehiro, N., & Capozziello, S. 2015, *ApJ*, 800, 31, doi: [10.1088/0004-637X/800/1/31](https://doi.org/10.1088/0004-637X/800/1/31)
- Dainotti, M. G., Fabrizio Cardone, V., Capozziello, S., Ostrowski, M., & Willingale, R. 2011, *ApJ*, 730, 135, doi: [10.1088/0004-637X/730/2/135](https://doi.org/10.1088/0004-637X/730/2/135)
- Dainotti, M. G., Hernandez, X., Postnikov, S., et al. 2017a, *ApJ*, 848, 88, doi: [10.3847/1538-4357/aa8a6b](https://doi.org/10.3847/1538-4357/aa8a6b)
- Dainotti, M. G., Lenart, A. L., Chraya, A., et al. 2023, *MNRAS*, 518, 2201, doi: [10.1093/mnras/stac2752](https://doi.org/10.1093/mnras/stac2752)
- Dainotti, M. G., Lenart, A. L., Sarracino, G., et al. 2020a, *ApJ*, 904, 97, doi: [10.3847/1538-4357/abbe8a](https://doi.org/10.3847/1538-4357/abbe8a)
- Dainotti, M. G., Nagataki, S., Maeda, K., Postnikov, S., & Pian, E. 2017b, *A&A*, 600, A98, doi: [10.1051/0004-6361/201628384](https://doi.org/10.1051/0004-6361/201628384)
- Dainotti, M. G., Nielson, V., Sarracino, G., et al. 2022c, *MNRAS*, 514, 1828, doi: [10.1093/mnras/stac1141](https://doi.org/10.1093/mnras/stac1141)
- Dainotti, M. G., Petrosian, V., Singal, J., & Ostrowski, M. 2013, *ApJ*, 774, 157, doi: [10.1088/0004-637X/774/2/157](https://doi.org/10.1088/0004-637X/774/2/157)
- Dainotti, M. G., Postnikov, S., Hernandez, X., & Ostrowski, M. 2016, *ApJL*, 825, L20, doi: [10.3847/2041-8205/825/2/L20](https://doi.org/10.3847/2041-8205/825/2/L20)
- Dainotti, M. G., Livermore, S., Kann, D. A., et al. 2020b, *ApJL*, 905, L26, doi: [10.3847/2041-8213/abcda9](https://doi.org/10.3847/2041-8213/abcda9)
- Dainotti, M. G., Young, S., Li, L., et al. 2022d, *ApJS*, 261, 25, doi: [10.3847/1538-4365/ac7c64](https://doi.org/10.3847/1538-4365/ac7c64)
- Dainotti, M. G., Narendra, A., Pollo, A., et al. 2024a, *ApJL*, 967, L30, doi: [10.3847/2041-8213/ad4970](https://doi.org/10.3847/2041-8213/ad4970)
- Dainotti, M. G., Taira, E., Wang, E., et al. 2024b, *ApJS*, 271, 22, doi: [10.3847/1538-4365/ad1aaf](https://doi.org/10.3847/1538-4365/ad1aaf)
- Dainotti, M. G., Bhardwaj, S., Cook, C., et al. 2025, *ApJS*, 277, 31, doi: [10.3847/1538-4365/adafa9](https://doi.org/10.3847/1538-4365/adafa9)
- de Barra, C., Meegan, C., & Fermi GBM Team. 2023, *GRB Coordinates Network*, 35131, 1
- Deng, C., Huang, Y.-F., & Xu, F. 2023, *ApJ*, 943, 126, doi: [10.3847/1538-4357/acaefd](https://doi.org/10.3847/1538-4357/acaefd)
- Dermer, C. D., Chiang, J., & Böttcher, M. 1999, *ApJ*, 513, 656, doi: [10.1086/306871](https://doi.org/10.1086/306871)
- Dong, X. F., Zhang, Z. B., Li, Q. M., Huang, Y. F., & Bian, K. 2023, *ApJ*, 958, 37, doi: [10.3847/1538-4357/acf852](https://doi.org/10.3847/1538-4357/acf852)
- Efron, B., & Petrosian, V. 1992, *ApJ*, 399, 345, doi: [10.1086/171931](https://doi.org/10.1086/171931)
- Fletcher, C., Meegan, C., & Fermi Gamma-ray Burst Monitor Team. 2024, *GRB Coordinates Network*, 35693, 1
- Fletcher, C., Veres, P., & Fermi-GBM Team. 2020, *GRB Coordinates Network*, 28663, 1
- Frederiks, D., Lysenko, A., Ridnaia, A., et al. 2023, *GRB Coordinates Network*, 35359, 1
- Frederiks, D., Lysenko, A., Ridnaya, A., et al. 2022, *GRB Coordinates Network*, 32472, 1
- Frederiks, D., Golenetskii, S., Aptekar, R., et al. 2018, *GRB Coordinates Network*, 22546, 1
- , 2019, *GRB Coordinates Network*, 26576, 1
- Frederiks, D., Golenetskii, S., Lysenko, A., et al. 2021a, *GRB Coordinates Network*, 29517, 1
- , 2021b, *GRB Coordinates Network*, 30694, 1
- Gao, H.-X., Geng, J.-J., Wu, X.-F., et al. 2024, *arXiv e-prints*, arXiv:2410.21687, doi: [10.48550/arXiv.2410.21687](https://doi.org/10.48550/arXiv.2410.21687)
- Gehrels, N., Chincarini, G., Giommi, P., et al. 2004, *ApJ*, 611, 1005, doi: [10.1086/422091](https://doi.org/10.1086/422091)
- Gehrels, N., Sarazin, C. L., O'Brien, P. T., et al. 2005, *Nature*, 437, 851, doi: [10.1038/nature04142](https://doi.org/10.1038/nature04142)
- Gehrels, N., Norris, J. P., Barthelmy, S. D., et al. 2006, *Nature*, 444, 1044, doi: [10.1038/nature05376](https://doi.org/10.1038/nature05376)
- Geng, J.-J., Hu, D.-F., Gao, H.-X., et al. 2025, *arXiv e-prints*, arXiv:2503.17766, doi: [10.48550/arXiv.2503.17766](https://doi.org/10.48550/arXiv.2503.17766)

- Ghirlanda, G., Ghisellini, G., Firmani, C., Celotti, A., & Bosnjak, Z. 2005, *MNRAS*, 360, L45, doi: [10.1111/j.1745-3933.2005.00043.x](https://doi.org/10.1111/j.1745-3933.2005.00043.x)
- Golenetskii, S., Aptekar, R., Mazets, E., et al. 2009, *GRB Coordinates Network*, 10045, 1
- Granut, J., Panaitescu, A., Kumar, P., & Woosley, S. E. 2002, *ApJL*, 570, L61, doi: [10.1086/340991](https://doi.org/10.1086/340991)
- Granut, J., Ramirez-Ruiz, E., & Perna, R. 2005, *ApJ*, 630, 1003, doi: [10.1086/431477](https://doi.org/10.1086/431477)
- Greiner, J., Krühler, T., Fynbo, J. P. U., et al. 2009, *ApJ*, 693, 1610, doi: [10.1088/0004-637X/693/2/1610](https://doi.org/10.1088/0004-637X/693/2/1610)
- Gruber, D., Goldstein, A., Weller von Ahlefeld, V., et al. 2014, *ApJS*, 211, 12, doi: [10.1088/0067-0049/211/1/12](https://doi.org/10.1088/0067-0049/211/1/12)
- Hamburg, R., Malacaria, C., Meegan, C., & Fermi GBM Team. 2020, *GRB Coordinates Network*, 29140, 1
- Hamburg, R., Veres, P., Meegan, C., et al. 2019, *GRB Coordinates Network*, 23707, 1
- Heise, J., Zand, J. I., Kippen, R. M., & Woods, P. M. 2001, in *Gamma-ray Bursts in the Afterglow Era*, ed. E. Costa, F. Frontera, & J. Hjorth, 16, doi: [10.1007/10853853\\_4](https://doi.org/10.1007/10853853_4)
- Hu, J.-P., & Wang, F.-Y. 2023, *Universe*, 9, 94, doi: [10.3390/universe9020094](https://doi.org/10.3390/universe9020094)
- Huang, Y. F., Dai, Z. G., & Lu, T. 2002, *MNRAS*, 332, 735, doi: [10.1046/j.1365-8711.2002.05334.x](https://doi.org/10.1046/j.1365-8711.2002.05334.x)
- Hui, C. M. 2019, *GRB Coordinates Network*, 24002, 1
- Jenke, P. 2013, *GRB Coordinates Network*, 15261, 1
- Jia, X. D., Hu, J. P., Yang, J., Zhang, B. B., & Wang, F. Y. 2022, *MNRAS*, 516, 2575, doi: [10.1093/mnras/stac2356](https://doi.org/10.1093/mnras/stac2356)
- Jin, Z.-P., Hotokezaka, K., Li, X., et al. 2016, *Nature Communications*, 7, 12898, doi: [10.1038/ncomms12898](https://doi.org/10.1038/ncomms12898)
- Katsukura, D., Sakamoto, T., Tashiro, M. S., & Terada, Y. 2020, *ApJ*, 889, 110, doi: [10.3847/1538-4357/ab6167](https://doi.org/10.3847/1538-4357/ab6167)
- Kippen, R. M., Woods, P. M., Heise, J., et al. 2003, in *American Institute of Physics Conference Series*, Vol. 662, *Gamma-Ray Burst and Afterglow Astronomy 2001: A Workshop Celebrating the First Year of the HETE Mission*, ed. G. R. Ricker & R. K. Vanderspek (AIP), 244–247, doi: [10.1063/1.1579349](https://doi.org/10.1063/1.1579349)
- Kippen, R. M., Woods, P. M., Heise, J., et al. 2001, in *Gamma-ray Bursts in the Afterglow Era*, ed. E. Costa, F. Frontera, & J. Hjorth, 22, doi: [10.1007/10853853\\_5](https://doi.org/10.1007/10853853_5)
- Lamb, D. Q., Donaghy, T. Q., & Graziani, C. 2004a, *NewAR*, 48, 459, doi: [10.1016/j.newar.2003.12.030](https://doi.org/10.1016/j.newar.2003.12.030)
- . 2005, *ApJ*, 620, 355, doi: [10.1086/426099](https://doi.org/10.1086/426099)
- Lamb, D. Q., Ricker, G. R., Atteia, J. L., et al. 2004b, *NewAR*, 48, 423, doi: [10.1016/j.newar.2003.12.042](https://doi.org/10.1016/j.newar.2003.12.042)
- Lenart, A. L., Dainotti, M. G., Khatiya, N., et al. 2025, *Journal of High Energy Astrophysics*, 47, 100384, doi: [10.1016/j.jheap.2025.100384](https://doi.org/10.1016/j.jheap.2025.100384)
- Lesage, S., Meegan, C., & Fermi Gamma-ray Burst Monitor Team. 2021, *GRB Coordinates Network*, 30573, 1
- . 2022a, *GRB Coordinates Network*, 31360, 1
- . 2022b, *GRB Coordinates Network*, 33112, 1
- Lesage, S., Meegan, C., & Fermi GBM Team. 2020a, *GRB Coordinates Network*, 28748, 1
- . 2020b, *GRB Coordinates Network*, 28326, 1
- Lesage, S., Poolakkil, S., Fletcher, C., et al. 2019, *GRB Coordinates Network*, 25575, 1
- Levine, D., Dainotti, M., Zvonarek, K. J., et al. 2022, *ApJ*, 925, 15, doi: [10.3847/1538-4357/ac4221](https://doi.org/10.3847/1538-4357/ac4221)
- Li, J.-L., Yang, Y.-P., Yi, S.-X., et al. 2024a, *A&A*, 689, A165, doi: [10.1051/0004-6361/202348542](https://doi.org/10.1051/0004-6361/202348542)
- Li, M. L., Ho, A. Y. Q., Ryan, G., et al. 2024b, *arXiv e-prints*, arXiv:2411.07973, doi: [10.48550/arXiv.2411.07973](https://doi.org/10.48550/arXiv.2411.07973)
- Li, X.-J., Zhang, Z.-B., Huang, Y.-F., & Xu, F. 2024c, *ApJ*, 962, 117, doi: [10.3847/1538-4357/ad18a8](https://doi.org/10.3847/1538-4357/ad18a8)
- Li, X. J., Zhang, Z. B., Zhang, X. L., & Zhen, H. Y. 2021, *ApJS*, 252, 16, doi: [10.3847/1538-4365/abd3fd](https://doi.org/10.3847/1538-4365/abd3fd)
- Liang, E., Zhang, B., Virgili, F., & Dai, Z. G. 2007, *ApJ*, 662, 1111, doi: [10.1086/517959](https://doi.org/10.1086/517959)
- Liang, N., Li, Z., Xie, X., & Wu, P. 2022, *ApJ*, 941, 84, doi: [10.3847/1538-4357/aca08a](https://doi.org/10.3847/1538-4357/aca08a)
- Lien, A., Sakamoto, T., Barthelmy, S. D., et al. 2016, *ApJ*, 829, 7, doi: [10.3847/0004-637X/829/1/7](https://doi.org/10.3847/0004-637X/829/1/7)
- Malacaria, C., Fletcher, C., Meegan, C., & Fermi GBM Team. 2021a, *GRB Coordinates Network*, 29246, 1
- Malacaria, C., Hristov, B., & Fermi GBM Team. 2021b, *GRB Coordinates Network*, 30199, 1
- Malacaria, C., Veres, P., Meegan, C., Bissaldi, E., & Fermi GBM Team. 2020, *GRB Coordinates Network*, 29073, 1
- Minaev, P. Y., & Pozanenko, A. S. 2020, *MNRAS*, 492, 1919, doi: [10.1093/mnras/stz3611](https://doi.org/10.1093/mnras/stz3611)
- Mochkovitch, R., Daigne, F., Barraud, C., & Atteia, J. L. 2004, in *Astronomical Society of the Pacific Conference Series*, Vol. 312, *Gamma-Ray Bursts in the Afterglow Era*, ed. M. Feroci, F. Frontera, N. Masetti, & L. Piro, 381, doi: [10.48550/arXiv.astro-ph/0303289](https://doi.org/10.48550/arXiv.astro-ph/0303289)
- Morgan, A. N., Long, J., Richards, J. W., et al. 2012, *ApJ*, 746, 170, doi: [10.1088/0004-637X/746/2/170](https://doi.org/10.1088/0004-637X/746/2/170)
- Myers, A., & Fermi Gamma-ray Burst Monitor Team. 2024, *GRB Coordinates Network*, 36120, 1
- Narayana Bhat, P., Meegan, C. A., von Kienlin, A., et al. 2016, *ApJS*, 223, 28, doi: [10.3847/0067-0049/223/2/28](https://doi.org/10.3847/0067-0049/223/2/28)
- Narendra, A., Dainotti, M., Sarkar, M., et al. 2024, *arXiv e-prints*, arXiv:2410.13985, doi: [10.48550/arXiv.2410.13985](https://doi.org/10.48550/arXiv.2410.13985)
- Norris, J. P., Nemiroff, R. J., Bonnell, J. T., et al. 1996, *ApJ*, 459, 393, doi: [10.1086/176902](https://doi.org/10.1086/176902)
- O'Connor, B., Beniamini, P., & Gill, R. 2024, *MNRAS*, 533, 1629, doi: [10.1093/mnras/stae1941](https://doi.org/10.1093/mnras/stae1941)
- Pe'er, A., Mészáros, P., & Rees, M. J. 2006, *ApJ*, 642, 995, doi: [10.1086/501424](https://doi.org/10.1086/501424)

- Planck Collaboration, Ade, P. A. R., Aghanim, N., et al. 2016, *A&A*, 594, A13, doi: [10.1051/0004-6361/201525830](https://doi.org/10.1051/0004-6361/201525830)
- Poolakkil, S., Meegan, C., & Fermi GBM Team. 2019, GRB Coordinates Network, 25130, 1
- . 2021, GRB Coordinates Network, 30279, 1
- . 2022, GRB Coordinates Network, 32089, 1
- Ramirez-Ruiz, E. 2005, *MNRAS*, 363, L61, doi: [10.1111/j.1745-3933.2005.00089.x](https://doi.org/10.1111/j.1745-3933.2005.00089.x)
- Rhoads, J. E. 1997, *ApJL*, 487, L1, doi: [10.1086/310876](https://doi.org/10.1086/310876)
- Ridnaia, A., Frederiks, D., Lysenko, A., et al. 2024, GRB Coordinates Network, 37139, 1
- Sakamoto, T., Lamb, D. Q., Kawai, N., et al. 2005, *ApJ*, 629, 311, doi: [10.1086/431235](https://doi.org/10.1086/431235)
- Sakamoto, T., Barbier, L., Barthelmy, S. D., et al. 2006, *ApJL*, 636, L73, doi: [10.1086/500261](https://doi.org/10.1086/500261)
- Sakamoto, T., Barthelmy, S. D., Barbier, L., et al. 2008, *ApJS*, 175, 179, doi: [10.1086/523646](https://doi.org/10.1086/523646)
- Sharma, V., Meegan, C., & Fermi Gamma-ray Burst Monitor Team. 2024, GRB Coordinates Network, 37301, 1
- Smith, J., Meegan, C., & Fermi Gamma-ray Burst Monitor Team. 2024, GRB Coordinates Network, 37478, 1
- Stanbro, M., Hui, C. M., & Meegan, C. 2017, GRB Coordinates Network, 22277, 1
- Sun, T.-R., Geng, J.-J., Yan, J.-Z., et al. 2024, *ApJL*, 976, L20, doi: [10.3847/2041-8213/ad85da](https://doi.org/10.3847/2041-8213/ad85da)
- Svinkin, D., Frederiks, D., Ulanov, M., et al. 2024, GRB Coordinates Network, 36584, 1
- Svinkin, D., Golenetskii, S., Aptekar, R., et al. 2019, GRB Coordinates Network, 25974, 1
- Tang, C.-H., Huang, Y.-F., Geng, J.-J., & Zhang, Z.-B. 2019, *ApJS*, 245, 1, doi: [10.3847/1538-4365/ab4711](https://doi.org/10.3847/1538-4365/ab4711)
- Tian, X., Li, J.-L., Yi, S.-X., et al. 2023, *ApJ*, 958, 74, doi: [10.3847/1538-4357/acfed8](https://doi.org/10.3847/1538-4357/acfed8)
- Tripp, R. 1998, *A&A*, 331, 815
- Tsvetkova, A., Frederiks, D., Golenetskii, S., et al. 2017, *ApJ*, 850, 161, doi: [10.3847/1538-4357/aa96af](https://doi.org/10.3847/1538-4357/aa96af)
- Tsvetkova, A., Golenetskii, S., Aptekar, R., et al. 2019, GRB Coordinates Network, 23637, 1
- Tsvetkova, A., Frederiks, D., Svinkin, D., et al. 2021, *ApJ*, 908, 83, doi: [10.3847/1538-4357/abd569](https://doi.org/10.3847/1538-4357/abd569)
- Ukwatta, T. N., Woźniak, P. R., & Gehrels, N. 2016, *MNRAS*, 458, 3821, doi: [10.1093/mnras/stw559](https://doi.org/10.1093/mnras/stw559)
- Urata, Y., Huang, K., Yamazaki, R., & Sakamoto, T. 2015, *ApJ*, 806, 222, doi: [10.1088/0004-637X/806/2/222](https://doi.org/10.1088/0004-637X/806/2/222)
- van Putten, M. H. P. M., Lee, G. M., Della Valle, M., Amati, L., & Levinson, A. 2014, *MNRAS*, 444, L58, doi: [10.1093/mnras/slu113](https://doi.org/10.1093/mnras/slu113)
- Veres, P. 2018, GRB Coordinates Network, 23352, 1
- Veres, P., & Fermi-GBM Team. 2020, GRB Coordinates Network, 29110, 1
- . 2022, GRB Coordinates Network, 31487, 1
- Veres, P., Fletcher, C., Meegan, C., & Fermi Gamma-ray Burst Monitor Team. 2023, GRB Coordinates Network, 34501, 1
- Veres, P., Hristov, B., Fletcher, C., Meegan, C., & Fermi GBM Team. 2021a, GRB Coordinates Network, 30233, 1
- Veres, P., Meegan, C., & Fermi Gamma-ray Burst Monitor Team. 2024, GRB Coordinates Network, 35755, 1
- Veres, P., Meegan, C., & Mailyan, B. 2018, GRB Coordinates Network, 23053, 1
- Veres, P., Roberts, O. J., & Fermi-GBM Team. 2021b, GRB Coordinates Network, 30779, 1
- Villasenor, J. S., Lamb, D. Q., Ricker, G. R., et al. 2005, *Nature*, 437, 855, doi: [10.1038/nature04213](https://doi.org/10.1038/nature04213)
- von Kienlin, A. 2008, GRB Coordinates Network, 8505, 1
- . 2018, GRB Coordinates Network, 23320, 1
- von Kienlin, A., Meegan, C. A., Paciesas, W. S., et al. 2014, *ApJS*, 211, 13, doi: [10.1088/0067-0049/211/1/13](https://doi.org/10.1088/0067-0049/211/1/13)
- . 2020, *ApJ*, 893, 46, doi: [10.3847/1538-4357/ab7a18](https://doi.org/10.3847/1538-4357/ab7a18)
- Wang, F. Y., Hu, J. P., Zhang, G. Q., & Dai, Z. G. 2022, *ApJ*, 924, 97, doi: [10.3847/1538-4357/ac3755](https://doi.org/10.3847/1538-4357/ac3755)
- Wang, J., Xin, L. P., Qiu, Y. L., et al. 2024, *Research in Astronomy and Astrophysics*, 24, 115006, doi: [10.1088/1674-4527/ad7fb5](https://doi.org/10.1088/1674-4527/ad7fb5)
- Wang, J. S., Wang, F. Y., Cheng, K. S., & Dai, Z. G. 2016, *A&A*, 585, A68, doi: [10.1051/0004-6361/201526485](https://doi.org/10.1051/0004-6361/201526485)
- Wei, J., Cordier, B., Antier, S., et al. 2016, arXiv e-prints, arXiv:1610.06892, doi: [10.48550/arXiv.1610.06892](https://doi.org/10.48550/arXiv.1610.06892)
- Wood, J., & Fermi GBM Team. 2021, GRB Coordinates Network, 30490, 1
- Xu, F., Huang, Y.-F., & Geng, J.-J. 2023a, *A&A*, 679, A103, doi: [10.1051/0004-6361/202346674](https://doi.org/10.1051/0004-6361/202346674)
- Xu, F., Huang, Y.-F., Geng, J.-J., et al. 2023b, *A&A*, 673, A20, doi: [10.1051/0004-6361/202245414](https://doi.org/10.1051/0004-6361/202245414)
- Xu, F., Tang, C.-H., Geng, J.-J., et al. 2021, *ApJ*, 920, 135, doi: [10.3847/1538-4357/ac158a](https://doi.org/10.3847/1538-4357/ac158a)
- Xu, M., & Huang, Y. F. 2012, *A&A*, 538, A134, doi: [10.1051/0004-6361/201117754](https://doi.org/10.1051/0004-6361/201117754)
- Yamazaki, R., Ioka, K., & Nakamura, T. 2002, *ApJL*, 571, L31, doi: [10.1086/341225](https://doi.org/10.1086/341225)
- . 2004, *ApJL*, 607, L103, doi: [10.1086/421872](https://doi.org/10.1086/421872)
- Yamazaki, R., Yonetoku, D., & Nakamura, T. 2003, *ApJL*, 594, L79, doi: [10.1086/378736](https://doi.org/10.1086/378736)
- Ye, X.-M., Wei, D.-M., Zhu, Y.-M., & Jin, Z.-P. 2024, *Research in Astronomy and Astrophysics*, 24, 045011, doi: [10.1088/1674-4527/ad2b39](https://doi.org/10.1088/1674-4527/ad2b39)
- Yin, Y.-H. I., Zhang, B.-B., Yang, J., et al. 2024, *ApJL*, 975, L27, doi: [10.3847/2041-8213/ad8652](https://doi.org/10.3847/2041-8213/ad8652)
- Yonetoku, D., Murakami, T., Nakamura, T., et al. 2004, *ApJ*, 609, 935, doi: [10.1086/421285](https://doi.org/10.1086/421285)
- Younes, G., & Bhat, P. N. 2013, GRB Coordinates Network, 14219, 1

- Yuan, W., Zhang, C., Chen, Y., & Ling, Z. 2022, in Handbook of X-ray and Gamma-ray Astrophysics, ed. C. Bambi & A. Sanganello (Springer Singapore), 86, doi: [10.1007/978-981-16-4544-0\\_151-1](https://doi.org/10.1007/978-981-16-4544-0_151-1)
- Zhang, B., Dai, X., Lloyd-Ronning, N. M., & Mészáros, P. 2004, ApJL, 601, L119, doi: [10.1086/382132](https://doi.org/10.1086/382132)
- Zhang, B., Fan, Y. Z., Dyks, J., et al. 2006, ApJ, 642, 354, doi: [10.1086/500723](https://doi.org/10.1086/500723)
- Zhang, B., & Mészáros, P. 2002, ApJ, 581, 1236, doi: [10.1086/344338](https://doi.org/10.1086/344338)
- Zhang, B.-B., Zhang, B., Liang, E.-W., et al. 2011, ApJ, 730, 141, doi: [10.1088/0004-637X/730/2/141](https://doi.org/10.1088/0004-637X/730/2/141)
- Zhang, W., Yuan, W., Ling, Z., et al. 2025, Science China Physics, Mechanics, and Astronomy, 68, 219511, doi: [10.1007/s11433-024-2524-4](https://doi.org/10.1007/s11433-024-2524-4)
- Zhao, L., Zhang, B., Gao, H., et al. 2019, ApJ, 883, 97, doi: [10.3847/1538-4357/ab38c4](https://doi.org/10.3847/1538-4357/ab38c4)
- Zhou, H., Chen, W., Sun, H., et al. 2024a, GRB Coordinates Network, 36691, 1
- Zhou, H., Wang, W. X., Hu, J. W., et al. 2024b, GRB Coordinates Network, 36997, 1

**Table 1.** 303 GRBs Detected by *Swift*.

Name	SR <sup>a</sup>	Redshift	$T_{90}$ (s)	$S(25 - 50 \text{ keV})^b$ ( $10^{-7} \text{ erg cm}^{-2}$ )	$S(50 - 100 \text{ keV})^b$ ( $10^{-7} \text{ erg cm}^{-2}$ )	$S(15 - 150 \text{ keV})^b$ ( $10^{-7} \text{ erg cm}^{-2}$ )	$F(15 - 150 \text{ keV})^c$ ( $10^{-7} \text{ erg cm}^{-2} \text{ s}^{-1}$ )	Type <sup>d</sup>
XRF 201015A	$2.03 \pm 1.71$	0.426	$9.78 \pm 3.47$	$0.66 \pm 0.24$	$0.32 \pm 0.24$	$1.97 \pm 0.63$	$0.78 \pm 0.22$	Long
XRF 190829A	$1.47 \pm 0.35$	0.079	$56.90 \pm 47.00$	$21.20 \pm 2.27$	$14.40 \pm 3.03$	$63.70 \pm 7.23$	$7.42 \pm 1.17$	Long
XRF 060923B	$1.38 \pm 0.36$	1.51	$8.95 \pm 1.30$	$1.62 \pm 0.19$	$1.17 \pm 0.27$	$4.90 \pm 0.63$	$0.74 \pm 0.19$	Long
XRF 210210A	$1.38 \pm 0.17$	0.715	$6.60 \pm 0.59$	$3.49 \pm 0.20$	$2.53 \pm 0.28$	$10.60 \pm 0.66$	$3.97 \pm 0.30$	Long
XRF 081007	$1.34 \pm 0.29$	0.529	$9.73 \pm 4.87$	$2.50 \pm 0.24$	$1.86 \pm 0.35$	$7.61 \pm 0.82$	$1.63 \pm 0.24$	Long
XRR 091018	$1.24 \pm 0.07$	0.971	$4.37 \pm 0.60$	$4.91 \pm 0.14$	$3.97 \pm 0.19$	$15.20 \pm 0.44$	$5.91 \pm 0.20$	Long
XRR 120815A	$1.23 \pm 0.32$	2.359	$7.23 \pm 2.52$	$1.59 \pm 0.20$	$1.29 \pm 0.29$	$4.92 \pm 0.69$	$1.41 \pm 0.23$	Long
XRR 090726	$1.22 \pm 0.26$	2.71	$56.68 \pm 12.17$	$2.53 \pm 0.24$	$2.08 \pm 0.39$	$7.86 \pm 0.89$	$0.53 \pm 0.13$	Long
XRR 100316B	$1.21 \pm 0.24$	1.18	$3.84 \pm 0.43$	$0.64 \pm 0.06$	$0.53 \pm 0.09$	$1.98 \pm 0.21$	$0.78 \pm 0.11$	Long
XRR 121211A	$1.20 \pm 0.34$	1.023	$182.70 \pm 38.73$	$4.06 \pm 0.50$	$3.38 \pm 0.85$	$12.70 \pm 1.88$	$0.98 \pm 0.28$	Long

**Notes.**

<sup>a</sup>SR is the fluence ratio of  $S(25 - 50 \text{ keV})/S(50 - 100 \text{ keV})$ .

<sup>b</sup>Energy fluence in the band of 25 – 50 keV ( $S(25 - 50 \text{ keV})$ ), 50 – 100 keV ( $S(50 - 100 \text{ keV})$ ), and 15 – 150 keV ( $S(15 - 150 \text{ keV})$ ). Data are taken from the BAT3 catalog (Lien et al. 2016).

<sup>c</sup>Peak energy flux in 15 – 150 keV band. Data are taken from the BAT3 catalog (Lien et al. 2016).

<sup>d</sup>Long or short GRBs as judged from the duration.

(This table is available in its entirety in machine-readable form.)

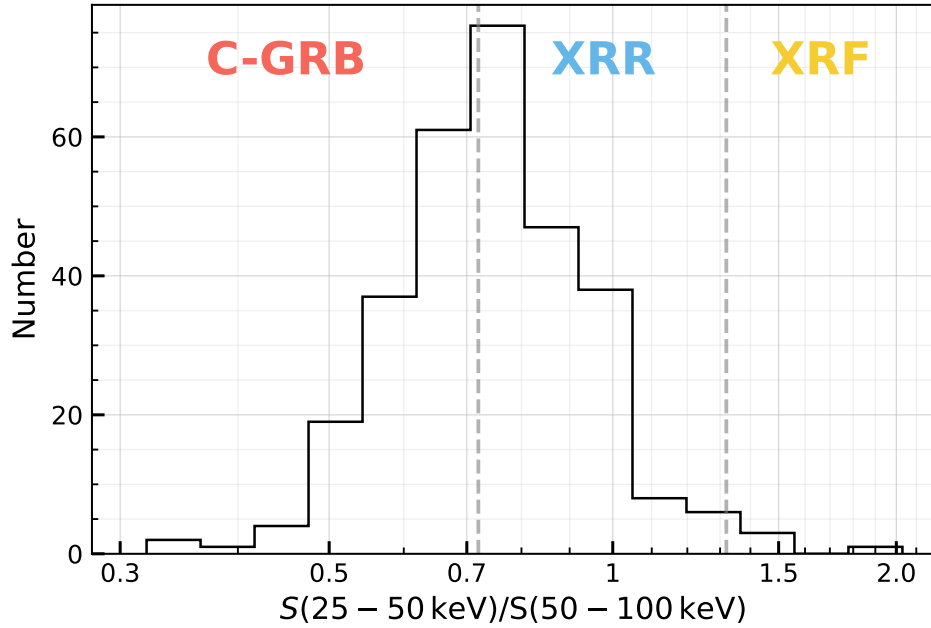


**Figure 1.** The distribution of the fluence ratio  $S(25 - 50 \text{ keV})/S(50 - 100 \text{ keV})$  for the whole sample. The vertical dashed lines correspond to the borders between C-GRBs and XRRs, and between XRRs and XRFs.

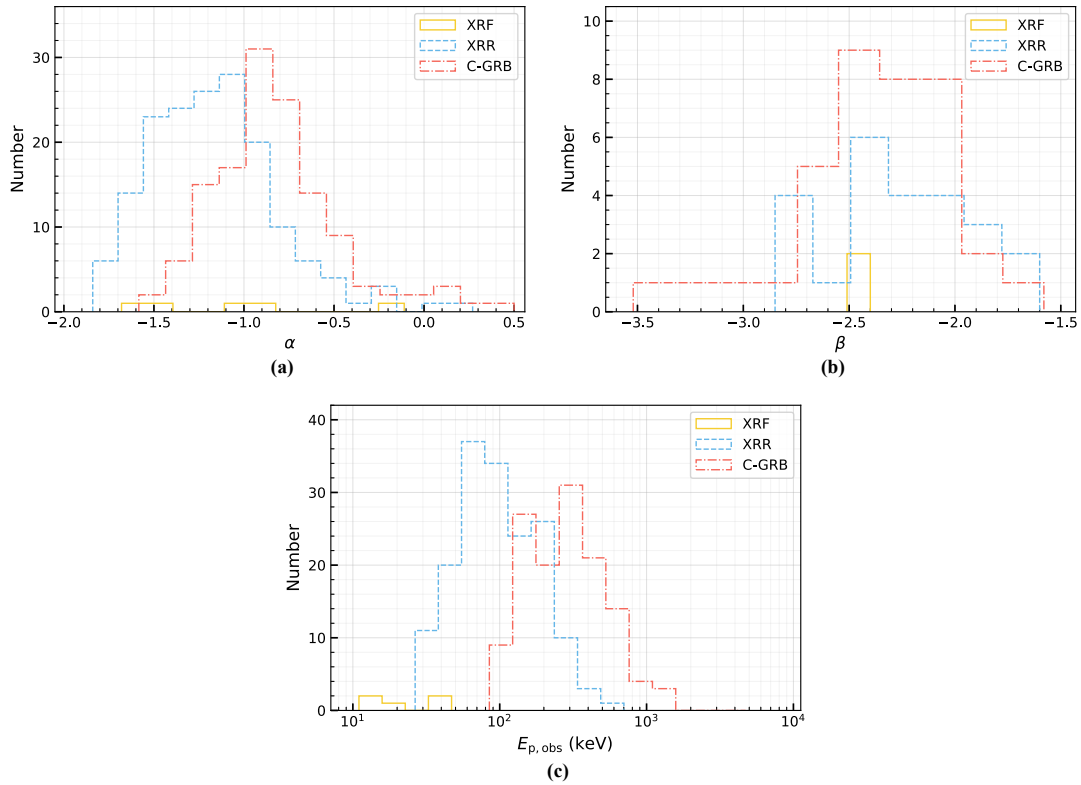


**Figure 2.** The distribution of  $\alpha$  (Panel (a)),  $\beta$  (Panel (b)), and  $E_{p,obs}$  (Panel (c)) for the whole sample. XRFs, XRRs, and C-GRBs are marked with yellow solid lines, blue dashed lines, and red dash-dotted lines, respectively.

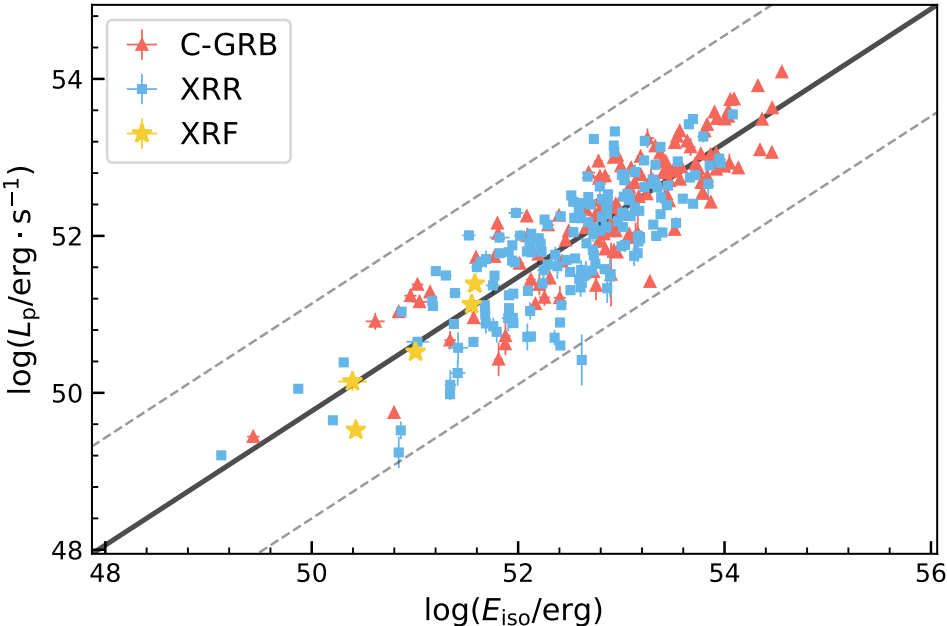


**Figure 3.** The best-fit  $E_{\text{iso}} - L_p$  correlation for the 303 GRBs in the sample. XRFs, XRRs, and C-GRBs are marked with yellow stars, blue squares, and red triangles, respectively. The black solid line is the best-fit curve for the observational data points. The gray dashed lines represent the  $3\sigma$  confidence level.

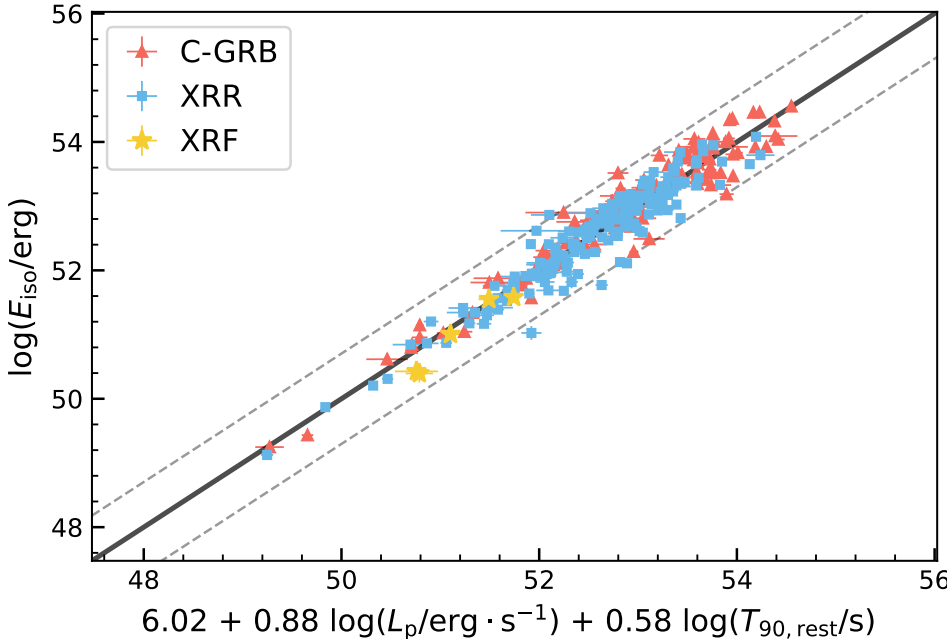


**Figure 4.** The best-fit  $L_p - T_{90,\text{rest}} - E_{\text{iso}}$  correlation for the 303 GRBs in the sample. XRFs, XRRs, and C-GRBs are marked with yellow stars, blue squares, and red triangles, respectively. The black solid line is the best-fit curve for the observational data points. The gray dashed lines mark the  $3\sigma$  confidence range.

**Table 2.** Spectral Parameters of the GRBs.

Name	$E_{p,obs}/\text{keV}$	$\alpha^a$	$\beta^b$	Spectra model <sup>c</sup>	Ref. <sup>d</sup>
XRF 201015A	$14 \pm 6$	-1.00 (fixed)	$-2.40 \pm 0.21$	BAND	4
XRF 190829A	$11 \pm 1$	$-0.92 \pm 0.62$	$-2.51 \pm 0.01$	BAND	5
XRF 060923B	$47 \pm 5.5$	$-0.11 \pm 0.79$		CPL	2
XRF 210210A	$16.6 \pm 9$	$-1.68 \pm 0.24$		CPL	6
XRF 081007	$40 \pm 10$	$-1.40 \pm 0.40$		CPL	7
XRR 091018	$28 \pm 13$	$-1.53 \pm 0.49$		CPL	8
XRR 120815A	$31 \pm 6.5$	$-0.87 \pm 0.72$		CPL	2
XRR 090726	$29 \pm 6$	$-1.03 \pm 0.59$		CPL	2
XRR 100316B	$31 \pm 14$	$-1.51 \pm 0.46$		CPL	2
XRR 121211A	$98.039 \pm 10.339$	$-0.22 \pm 0.31$		CPL	1

**Notes.**

<sup>a</sup>Low energy photon index.

<sup>b</sup>High energy photon index.

<sup>c</sup>The best-fit spectra model. BAND means the spectrum is best described by a Band function (Band et al. 1993), while CPL means the spectrum is best fitted by a cut-off power-law function.

<sup>d</sup>References of the spectral parameters. (1) *Fermi* online catalog, <https://heasarc.gsfc.nasa.gov/W3Browse/fermi/fermigbrst.html>; (2) *Konus-Wind* online catalog, <https://www.ioffe.ru/LEA/catalogs.html>; (3) The BAT3 catalog [https://swift.gsfc.nasa.gov/results/batgrbrcat/index\\_tables.html](https://swift.gsfc.nasa.gov/results/batgrbrcat/index_tables.html); (4) Fletcher et al. (2020); (5) Lesage et al. (2019); (6) Frederiks et al. (2021a); (7) Bissaldi et al. (2008a); (8) Golenetskii et al. (2009); (9) Fletcher et al. (2024); (10) Jenke (2013); (11) Stanbro et al. (2017); (12) Veres et al. (2018); (13) Poolakkil et al. (2022); (14) Bissaldi et al. (2019); (15) Veres & Fermi-GBM Team (2022); (16) Poolakkil et al. (2019); (17) Lesage et al. (2020a); (18) Smith et al. (2024); (19) Veres et al. (2024); (20) Svinkin et al. (2024); (21) von Kienlin (2008); (22) Younes & Bhat (2013); (23) Tsvetkova et al. (2019); (24) Hamburg et al. (2020); (25) Bissaldi et al. (2008b); (26) Wood & Fermi GBM Team (2021); (27) Malacaria et al. (2021a); (28) Veres et al. (2021b); (29) von Kienlin (2018); (30) Myers & Fermi Gamma-ray Burst Monitor Team (2024); (31) Hui (2019); (32) Malacaria et al. (2020); (33) Hamburg et al. (2019); (34) Veres et al. (2023); (35) Frederiks et al. (2022); (36) Veres et al. (2021a); (37) Poolakkil et al. (2021); (38) Veres & Fermi-GBM Team (2020); (39) de Barra et al. (2023); (40) Frederiks et al. (2021b); (41) Lesage et al. (2022a); (42) Sharma et al. (2024); (43) Veres (2018); (44) Frederiks et al. (2019); (45) Frederiks et al. (2018); (46) Lesage et al. (2022b); (47) Ridnaia et al. (2024); (48) Malacaria et al. (2021b); (49) Svinkin et al. (2019); (50) Frederiks et al. (2023); (51) Bissaldi et al. (2023); (52) Lesage et al. (2020b); (53) Lesage et al. (2021);

(This table is available in its entirety in machine-readable form.)

**Table 3.** Some Key Parameters of the GRBs.

Name	$\log(\text{SR})^a$	$\log(T_{90,\text{rest}}/s)^b$	$\log(E_{\text{iso}}/\text{erg})^c$	$\log(L_p/(\text{erg}/s))^c$	$\log(E_p/\text{keV})^d$
XRF 201015A	$0.31 \pm 0.36$	$0.84 \pm 0.15$	$50.39 \pm 0.14$	$50.14 \pm 0.12$	$1.30 \pm 0.19$
XRF 190829A	$0.17 \pm 0.10$	$1.72 \pm 0.36$	$50.55 \pm 0.05$	$49.65 \pm 0.07$	$1.07 \pm 0.04$
XRF 060923B	$0.14 \pm 0.11$	$0.55 \pm 0.06$	$51.55 \pm 0.06$	$51.13 \pm 0.11$	$2.07 \pm 0.05$
XRF 210210A	$0.14 \pm 0.05$	$0.59 \pm 0.04$	$51.58 \pm 0.03$	$51.39 \pm 0.03$	$1.45 \pm 0.24$
XRF 081007	$0.13 \pm 0.09$	$0.80 \pm 0.22$	$51.01 \pm 0.05$	$50.52 \pm 0.06$	$1.79 \pm 0.11$
XRR 091018	$0.09 \pm 0.02$	$0.35 \pm 0.06$	$51.91 \pm 0.01$	$51.79 \pm 0.01$	$1.74 \pm 0.20$
XRR 120815A	$0.09 \pm 0.11$	$0.33 \pm 0.15$	$52.02 \pm 0.06$	$52.00 \pm 0.07$	$2.02 \pm 0.09$
XRR 090726	$0.09 \pm 0.09$	$1.18 \pm 0.09$	$52.36 \pm 0.05$	$51.76 \pm 0.10$	$2.03 \pm 0.09$
XRR 100316B	$0.08 \pm 0.09$	$0.25 \pm 0.05$	$51.17 \pm 0.05$	$51.11 \pm 0.06$	$1.83 \pm 0.20$
XRR 121211A	$0.08 \pm 0.12$	$1.96 \pm 0.09$	$51.69 \pm 0.06$	$50.88 \pm 0.13$	$2.30 \pm 0.05$

**Notes.**

<sup>a</sup>The logarithm value of the fluence ratio of  $S(25 - 50 \text{ keV})/S(50 - 100 \text{ keV})$ .

<sup>b</sup>The rest frame burst duration, calculated with  $T_{90,\text{rest}} = T_{90}/(1+z)$ .

<sup>c</sup>Converted to the rest frame energy band of  $1 - 10^4 \text{ keV}$ .

<sup>d</sup>The rest frame peak energy, calculated with  $E_p = E_{p,\text{obs}} \times (1+z)$ .

(This table is available in its entirety in machine-readable form.)

**Table 4.** K-S Test Results.

Sub-samples	$E_{p,\text{obs}}$	$\alpha$	$\beta$	$\log(\text{SR})$	$\log(T_{90,\text{rest}})$	$\log(E_{\text{iso}})$	$\log(L_p)$	$\log(E_p)$
LGRB & SGRB	0.00032	3.10E-05		0.0038	1.60E-10	1.70E-11	0.00018	0.26
XRR & C-GRB	2.80E-22	3.70E-13	0.8	7.50E-88	0.1	4.70E-06	2.50E-07	1.10E-23
XRF & XRR	0.0002	0.65	0.34	1.70E-09	0.079	9.00E-05	0.0024	0.00011
XRF & C-GRB	5.60E-09	0.36	0.46	5.60E-09	0.094	2.40E-05	0.00024	1.20E-07

**Notes.** Pairwise comparison of various sub-samples. K-S test probability ( $P$ ) for different parameters are listed.

**Table 5.** The best-fit results of various correlations.

All GRBs							
Correlation form	$a$	$b$	$c$	$\sigma_{\text{in}}^a$	$\chi^2/\text{d.o.f.}^b$	$\rho^c$	$p^c$
$\log E_p = a + b \log L_p$	$-10.977 \pm 1.056$	$0.261 \pm 0.02$		$0.306 \pm 0.014$	0.108	0.61	7.80E-33
$\log E_p = a + b \log E_{\text{iso}}$	$-10.639 \pm 1.073$	$0.252 \pm 0.02$		$0.312 \pm 0.014$	0.113	0.61	9.40E-33
$\log L_p = a + b \log E_{\text{iso}}$	$7.085 \pm 1.49$	$0.854 \pm 0.028$		$0.456 \pm 0.019$	0.224	0.85	7.60E-84
$\log E_p = a + b \log \text{SR}$	$2.25 \pm 0.026$	$-2.914 \pm 0.158$		$0.21 \pm 0.012$	0.075	-0.74	1.30E-53
$\log E_{\text{iso}} = a + b \log \text{SR}$	$52.325 \pm 0.082$	$-2.881 \pm 0.529$		$0.872 \pm 0.037$	0.813	-0.36	6.10E-11
$\log L_p = a + b \log \text{SR}$	$51.689 \pm 0.081$	$-2.893 \pm 0.515$		$0.861 \pm 0.037$	0.796	-0.36	7.70E-11
$\log E_{\text{iso}} = a + b \log L_p + c \log T_{90,\text{rest}}$	$6.015 \pm 0.836$	$0.883 \pm 0.016$	$0.582 \pm 0.021$	$0.235 \pm 0.011$	0.065	0.95	6.20E-153
$\log E_p = a + b \log L_p + c \log T_{90,\text{rest}}$	$-11.047 \pm 1.058$	$0.262 \pm 0.02$	$0.041 \pm 0.028$	$0.306 \pm 0.014$	0.108	0.62	6.70E-34
$\log E_p = a + b \log E_{\text{iso}} + c \log T_{90,\text{rest}}$	$-12.486 \pm 1.126$	$0.29 \pm 0.022$	$-0.131 \pm 0.03$	$0.301 \pm 0.014$	0.107	0.63	2.50E-35
$\log E_p = a + b \log E_{\text{iso}} + c \log L_p$	$-11.773 \pm 1.069$	$0.108 \pm 0.039$	$0.168 \pm 0.04$	$0.303 \pm 0.014$	0.106	0.64	8.40E-36
$\log E_p = a + b \log E_{\text{iso}} + c \log \text{SR}$	$-7.057 \pm 0.772$	$0.177 \pm 0.015$	$-2.398 \pm 0.131$	$0.169 \pm 0.01$	0.052	0.84	2.70E-80
$\log E_p = a + b \log L_p + c \log \text{SR}$	$-6.771 \pm 0.792$	$0.174 \pm 0.015$	$-2.336 \pm 0.136$	$0.175 \pm 0.01$	0.051	0.84	1.50E-80
LGRBs only							
Correlation form	$a$	$b$	$c$	$\sigma_{\text{in}}^a$	$\chi^2/\text{d.o.f.}^b$	$\rho^c$	$p^c$
$\log E_p = a + b \log L_p$	$-23.336 \pm 0.798$	$0.496 \pm 0.015$		$0.278 \pm 0.014$	0.143	0.67	2.10E-37
$\log E_p = a + b \log E_{\text{iso}}$	$-23.477 \pm 0.823$	$0.493 \pm 0.016$		$0.271 \pm 0.014$	0.111	0.69	1.70E-41
$\log L_p = a + b \log E_{\text{iso}}$	$2.621 \pm 1.709$	$0.938 \pm 0.032$		$0.441 \pm 0.019$	0.209	0.84	2.20E-76
$\log E_p = a + b \log \text{SR}$	$2.235 \pm 0.027$	$-3.109 \pm 0.166$		$0.195 \pm 0.012$	0.063	-0.76	2.50E-53
$\log E_{\text{iso}} = a + b \log \text{SR}$	$52.323 \pm 0.068$	$-4.034 \pm 0.46$		$0.698 \pm 0.033$	0.54	-0.46	2.20E-16
$\log L_p = a + b \log \text{SR}$	$51.669 \pm 0.08$	$-3.705 \pm 0.52$		$0.8 \pm 0.037$	0.7	-0.42	1.20E-13
$\log E_{\text{iso}} = a + b \log L_p + c \log T_{90,\text{rest}}$	$6.372 \pm 0.893$	$0.876 \pm 0.017$	$0.602 \pm 0.026$	$0.226 \pm 0.011$	0.06	0.94	8.40E-138
$\log E_p = a + b \log L_p + c \log T_{90,\text{rest}}$	$-24.011 \pm 0.799$	$0.506 \pm 0.015$	$0.124 \pm 0.032$	$0.269 \pm 0.014$	0.081	0.68	2.20E-40
$\log E_p = a + b \log E_{\text{iso}} + c \log T_{90,\text{rest}}$	$-24.071 \pm 0.786$	$0.508 \pm 0.015$	$-0.177 \pm 0.03$	$0.251 \pm 0.013$	0.075	0.71	7.60E-44
$\log E_p = a + b \log E_{\text{iso}} + c \log L_p$	$-24.288 \pm 0.794$	$0.28 \pm 0.039$	$0.231 \pm 0.039$	$0.252 \pm 0.013$	0.074	0.71	4.00E-44
$\log E_p = a + b \log E_{\text{iso}} + c \log \text{SR}$	$-8.146 \pm 0.92$	$0.198 \pm 0.018$	$-2.274 \pm 0.153$	$0.165 \pm 0.01$	0.044	0.85	1.00E-81
$\log E_p = a + b \log L_p + c \log \text{SR}$	$-6.57 \pm 0.841$	$0.17 \pm 0.016$	$-2.391 \pm 0.153$	$0.169 \pm 0.01$	0.043	0.86	5.30E-82

**Notes.**<sup>a</sup>Intrinsic scatter of the correlation obtained from MCMC fitting.<sup>b</sup>The reduced  $\chi^2$  of the best-fit correlation.<sup>c</sup> $\rho$  and  $p$  represent the Spearman correlation coefficient and the corresponding chance probability, respectively.

**Table 6.** The best-fit results of various correlations after correcting redshift evolution.

All GRBs							
Correlation form <sup>a</sup>	<i>a</i>	<i>b</i>	<i>c</i>	$\sigma_{\text{in}}$	$\chi^2/\text{d.o.f.}$	$\rho$	<i>p</i>
$\log E'_p = a + b \log L'_p$	$-11.66 \pm 1.36$	$0.276 \pm 0.027$		$0.306 \pm 0.014$	0.109	0.5	5.50E-21
$\log E'_p = a + b \log E'_{\text{iso}}$	$-9.867 \pm 1.263$	$0.235 \pm 0.024$		$0.313 \pm 0.014$	0.112	0.49	1.80E-19
$\log L'_p = a + b \log E'_{\text{iso}}$	$15.125 \pm 1.67$	$0.685 \pm 0.032$		$0.425 \pm 0.018$	0.197	0.72	1.20E-49
$\log E'_p = a + b \log \text{SR}$	$1.924 \pm 0.022$	$-2.887 \pm 0.134$		$0.17 \pm 0.011$	0.055	-0.79	3.60E-65
$\log E'_{\text{iso}} = a + b \log \text{SR}$	$51.335 \pm 0.066$	$-2.556 \pm 0.434$		$0.71 \pm 0.031$	0.538	-0.37	2.20E-11
$\log L'_p = a + b \log \text{SR}$	$50.186 \pm 0.058$	$-2.404 \pm 0.373$		$0.623 \pm 0.027$	0.417	-0.41	1.30E-13
$\log E'_{\text{iso}} = a + b \log L'_p + c \log T'_{90,\text{rest}}$	$8.089 \pm 1.122$	$0.845 \pm 0.022$	$0.603 \pm 0.022$	$0.247 \pm 0.011$	0.071	0.92	1.90E-126
$\log E'_p = a + b \log L'_p + c \log T'_{90,\text{rest}}$	$-11.631 \pm 1.35$	$0.274 \pm 0.027$	$0.041 \pm 0.028$	$0.305 \pm 0.014$	0.108	0.51	1.80E-21
$\log E'_p = a + b \log E'_{\text{iso}} + c \log T'_{90,\text{rest}}$	$-13.338 \pm 1.463$	$0.307 \pm 0.029$	$-0.145 \pm 0.033$	$0.301 \pm 0.014$	0.107	0.52	1.60E-22
$\log E'_p = a + b \log E'_{\text{iso}} + c \log L'_p$	$-12.518 \pm 1.373$	$0.109 \pm 0.038$	$0.182 \pm 0.042$	$0.302 \pm 0.014$	0.106	0.52	9.70E-23
$\log E'_p = a + b \log E'_{\text{iso}} + c \log \text{SR}$	$-4.637 \pm 0.863$	$0.127 \pm 0.017$	$-2.532 \pm 0.128$	$0.154 \pm 0.01$	0.048	0.82	4.10E-74
$\log E'_p = a + b \log L'_p + c \log \text{SR}$	$-3.966 \pm 0.986$	$0.117 \pm 0.02$	$-2.515 \pm 0.141$	$0.164 \pm 0.01$	0.048	0.81	6.80E-73
LGRBs only							
Correlation form <sup>a</sup>	<i>a</i>	<i>b</i>	<i>c</i>	$\sigma_{\text{in}}$	$\chi^2/\text{d.o.f.}$	$\rho$	<i>p</i>
$\log E'_p = a + b \log L'_p$	$-21.186 \pm 1.35$	$0.459 \pm 0.027$		$0.273 \pm 0.018$	0.197	0.51	6.70E-20
$\log E'_p = a + b \log E'_{\text{iso}}$	$-16.961 \pm 1.123$	$0.368 \pm 0.022$		$0.259 \pm 0.018$	0.123	0.58	2.90E-26
$\log L'_p = a + b \log E'_{\text{iso}}$	$10.048 \pm 1.718$	$0.782 \pm 0.033$		$0.388 \pm 0.017$	0.166	0.76	2.30E-54
$\log E'_p = a + b \log \text{SR}$	$1.917 \pm 0.023$	$-2.965 \pm 0.144$		$0.162 \pm 0.01$	0.044	-0.8	1.00E-64
$\log E'_{\text{iso}} = a + b \log \text{SR}$	$51.329 \pm 0.058$	$-3.443 \pm 0.404$		$0.603 \pm 0.028$	0.398	-0.45	1.00E-15
$\log L'_p = a + b \log \text{SR}$	$50.168 \pm 0.06$	$-2.723 \pm 0.405$		$0.616 \pm 0.028$	0.409	-0.41	1.20E-12
$\log E'_{\text{iso}} = a + b \log L'_p + c \log T'_{90,\text{rest}}$	$8.201 \pm 1.11$	$0.842 \pm 0.022$	$0.605 \pm 0.027$	$0.236 \pm 0.011$	0.065	0.92	4.00E-118
$\log E'_p = a + b \log L'_p + c \log T'_{90,\text{rest}}$	$-21.305 \pm 1.324$	$0.459 \pm 0.026$	$0.084 \pm 0.049$	$0.271 \pm 0.018$	0.054	0.53	2.90E-22
$\log E'_p = a + b \log E'_{\text{iso}} + c \log T'_{90,\text{rest}}$	$-22.292 \pm 1.289$	$0.478 \pm 0.026$	$-0.241 \pm 0.036$	$0.219 \pm 0.016$	0.057	0.56	7.60E-25
$\log E'_p = a + b \log E'_{\text{iso}} + c \log L'_p$	$-21.56 \pm 1.293$	$0.165 \pm 0.04$	$0.298 \pm 0.052$	$0.225 \pm 0.016$	0.05	0.56	1.20E-24
$\log E'_p = a + b \log E'_{\text{iso}} + c \log \text{SR}$	$-5.507 \pm 0.975$	$0.144 \pm 0.019$	$-2.423 \pm 0.143$	$0.15 \pm 0.01$	0.038	0.84	1.40E-75
$\log E'_p = a + b \log L'_p + c \log \text{SR}$	$-3.559 \pm 0.971$	$0.109 \pm 0.019$	$-2.578 \pm 0.151$	$0.157 \pm 0.01$	0.039	0.83	2.80E-72

**Notes.**<sup>a</sup>The de-evolved parameters are denoted with the symbol '.

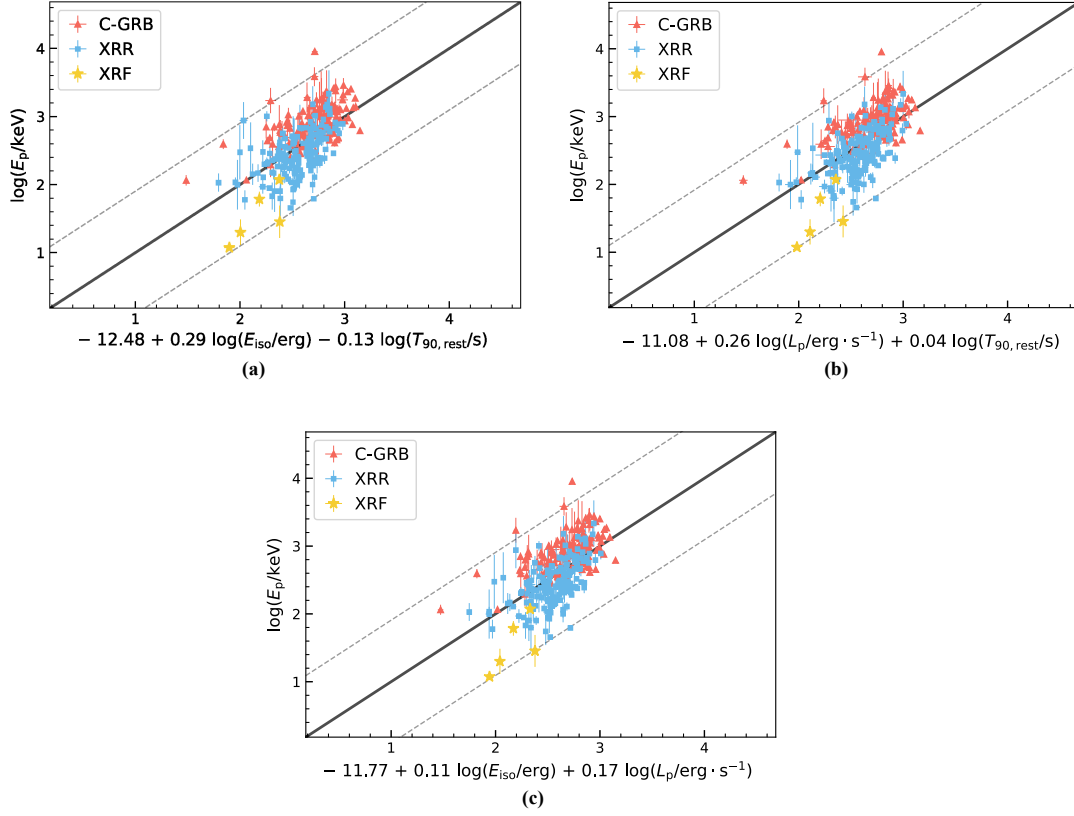


**Figure 5.** The best-fit results of the  $E_{\text{iso}} - T_{90,\text{rest}} - E_p$  correlation (Panel (a)),  $L_p - T_{90,\text{rest}} - E_p$  correlation (Panel (b)), and  $E_{\text{iso}} - L_p - E_p$  correlation (Panel (c)). XRFs, XRRs, and C-GRBs are marked with yellow stars, blue squares, and red triangles, respectively. The black solid lines represent the best-fit curves of the correlations. The gray dashed lines mark the  $3\sigma$  confidence range.

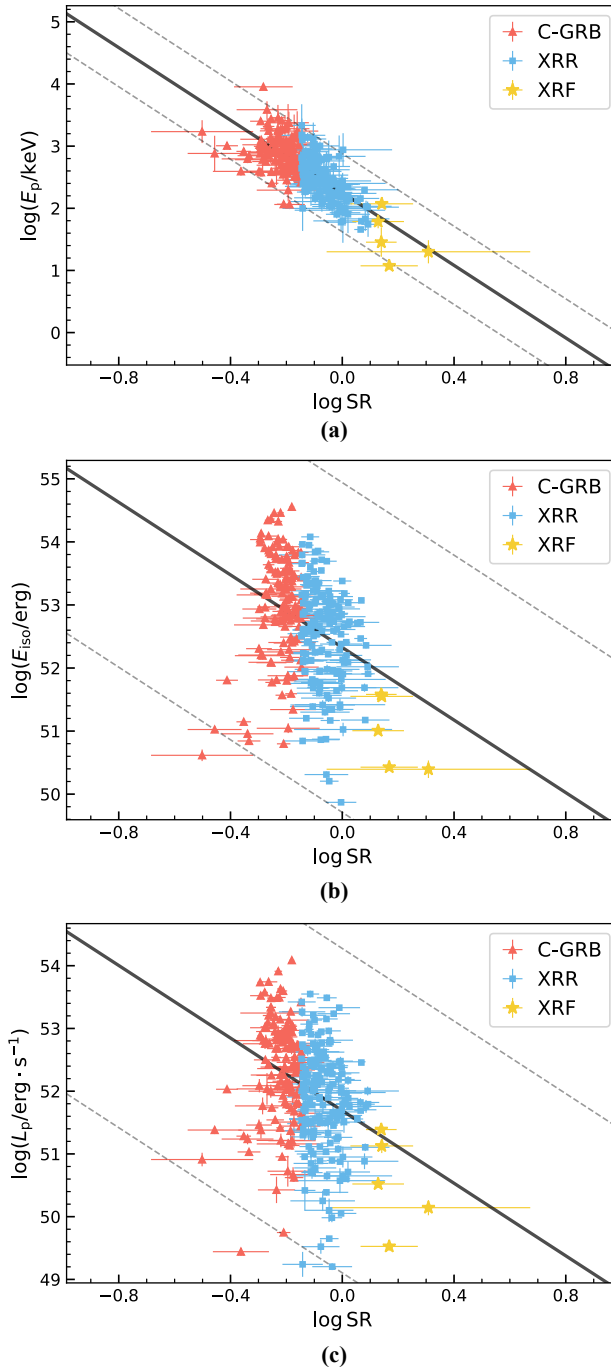


**Figure 6.** Dependence of  $E_p$ ,  $E_{\text{iso}}$ , and  $L_p$  on SR. Panel (a) shows  $E_p$  vs. SR. Panel (b) shows  $E_{\text{iso}}$  vs. SR. Panel (c) shows  $L_p$  vs. SR. XRFs are marked with yellow stars, XRRs with blue squares, and C-GRBs with red triangles. The black solid lines illustrate the best-fit curves of the correlations, and the gray dashed lines represent the  $3\sigma$  confidence interval.

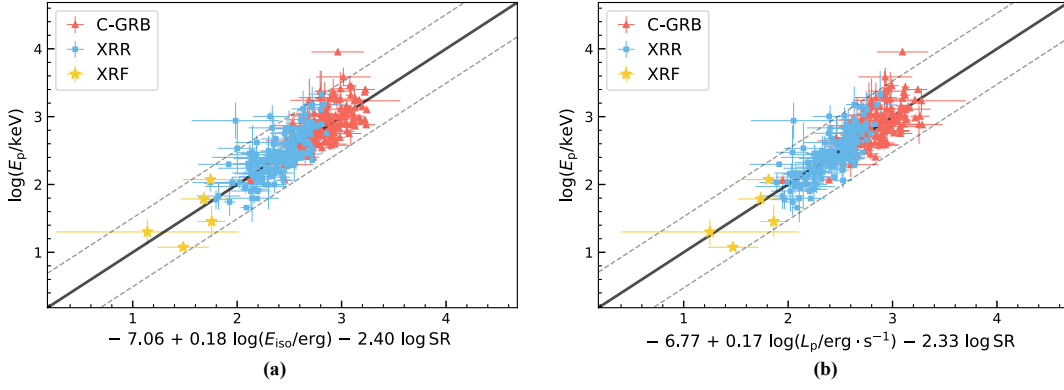


**Figure 7.** The best-fit  $E_{\text{iso}} - \text{SR} - E_p$  (Panel (a)) and  $L_p - \text{SR} - E_p$  (Panel (b)) correlations for all of the 303 GRBs in the sample. XRFs, XRRs, and C-GRBs are marked with yellow stars, blue squares, and red triangles, respectively. The black solid lines show the best-fit curves of the correlations, and the gray dashed lines mark the  $3\sigma$  confidence interval.

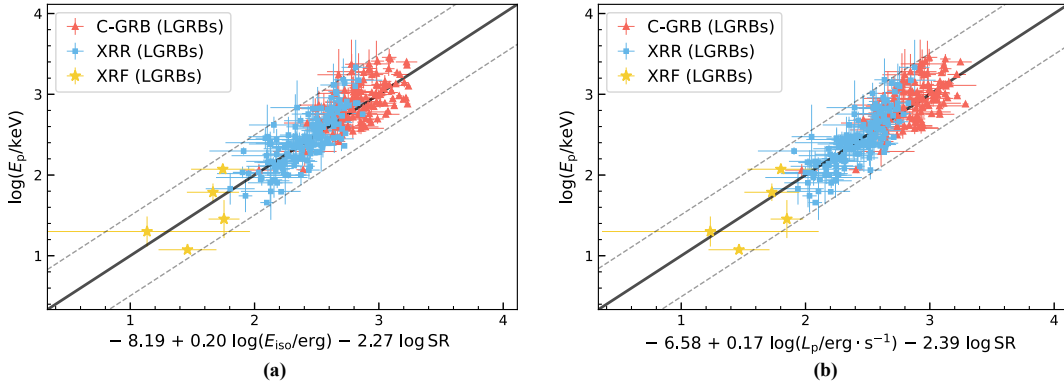


**Figure 8.** The best-fit  $E_{\text{iso}} - \text{SR} - E_p$  (Panel (a)) and  $L_p - \text{SR} - E_p$  (Panel (b)) correlations for 282 LGRBs in the sample. XRFs, XRRs, and C-GRBs are represented by yellow stars, blue squares, and red triangles, respectively. The black solid lines indicate the best-fit curves of the correlations, and the gray dashed lines denote the  $3\sigma$  confidence interval.

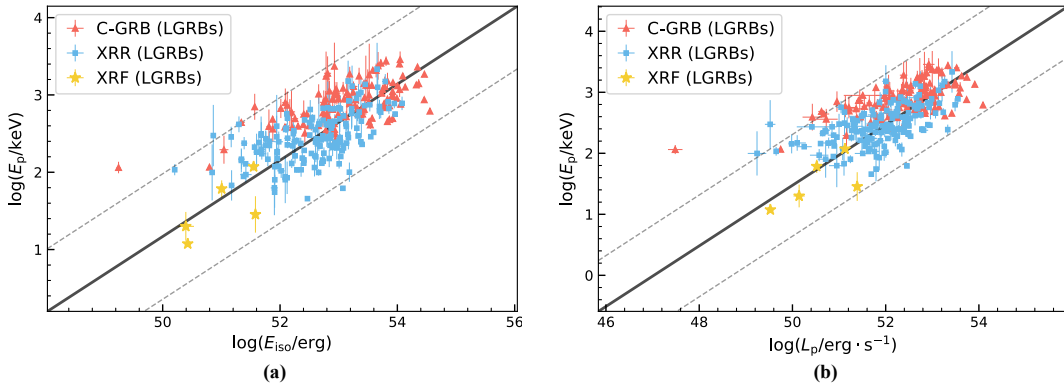


**Figure 9.** The best-fit results of  $E_{\text{iso}} - E_p$  and  $L_p - E_p$  correlations for LGRBs in the sample. The black solid lines indicate the best-fit curves of the correlations, and the gray dashed lines denote the  $3\sigma$  confidence range.